Transient behavior of the Asian summer monsoon anticyclone associated with eastward eddy shedding

Xinyue Wang[1,2], William Randel[2], Laura Pan[2], Yutian Wu[3], Pengfei Zhang[4]

[1]Advanced Study Program, National Center for Atmospheric Research, Boulder, CO, USA
[2]Atmospheric Chemistry Observations and Modeling Lab, National Center for Atmospheric Research, Boulder, CO, USA
[3]Lamont-Doherty Earth Observatory of Columbia University, Palisades, NY, USA
[4]Department of Meteorology and Atmospheric Science, Pennsylvania State University, University Park, PA, USA

Key Points:

- Eastward eddy shedding from the Asian monsoon anticyclone is often associated with the emergence of an isolated western Pacific anticyclone.
- Western Pacific anticyclone is closely related to the Silk Road pattern. Eddies grow along the jet in a baroclinically unstable background.
- Eastward eddy shedding occasionally occurs in association with the Pacific-Japan pattern forced by strong convection near the Philippines.

Abstract

The Asian monsoon anticyclone (AMA) exhibits a trimodal distribution of sub-vortices and the western Pacific is one of the preferred locations. Amplification of the western Pacific anticyclone (WPA) is often linked with eastward eddy shedding from the AMA, although the processes are not well understood. This study investigates the dynamics driving eastward eddy shedding associated with the emergence of the WPA in the upper troposphere and lower stratosphere on synoptic scales. Using reanalysis data during 1979 to 2019, our composite analysis reveals that amplified WPA events are closely related to the upstream Silk Road (SR) wave-train pattern over mid-latitude Eurasia as identified in previous studies. The quasi-stationary eastward propagating eddies result from baroclinic excitation along the westerly jet, as identified by coherent eddy heat fluxes and relaxation of the low-level temperature gradient. The upper-level westerly jet is important in determining the longitudinal phase-locking of wave trains, which are anchored and amplify near the jet exit. Occasionally enhanced convection near the Philippines also triggers anticyclonic eddies that propagate upward and northeastward via the Pacific-Japan (PJ) pattern, forming the WPA in the upper troposphere. Correlation analysis suggests that the SR and PJ mechanisms are not physically correlated.

1 Introduction

The Asian monsoon anticyclone (AMA) is the major circulation pattern in the upper troposphere and lower stratosphere (UTLS) during Northern summer, covering large parts of Eurasia. Relatively high tropospheric trace gases (e.g., water vapor, carbon monoxide, hydrogen cyanide) and aerosol (e.g., sulfate, black carbon) concentrations are confined within the area of anticyclonic circulation, imposing a substantial effect on UTLS composition, and also potentially on the surface weather and climate (Randel et al., 2015; X. Wang et al., 2018; Randel & Park, 2006; Randel et al., 2010; Santee et al., 2017; Höpfner et al., 2019; Vernier et al., 2015; Solomon et al., 2011; Y. Wu et al., 2020).

Understanding the location and movement of the AMA is important for quantifying dynamical and trace gas evolution in the UTLS. Studying the behavior of AMA dates back to Tao and Zhu (1964) who found the opposite movement between the upper-level AMA and mid-level western North Pacific subtropical high in East Asia. Previous studies assuming the anticyclone has a single center reveal that the AMA exhibits a bimodal distribution over Iran and the Tibetan Plateau (Q. Zhang et al., 2002). The details of the bimodal distribution are sensitive to the use of different reanalysis data sets (Nützel et al., 2016), and bimodality is potentially driven by variations in convection (e.g., Garny & Randel, 2013), monsoonal heating (e.g., P. Zhang et al., 2016), orographic effects (Q. Zhang et al., 2002; Liu et al., 2007), and large-scale dynamical variability (Amemiya & Sato, 2020). More recent analyses have highlighted that the AMA is subject to large dynamical variability on synoptic scales, constantly splitting, merging, and shedding anticyclonic eddies westward and eastward (Garny & Randel, 2013, 2016; Pan et al., 2016; P. M. Rupp & Haynes, 2020; Manney et al., 2021). C. J. Hsu and Plumb (2000) showed that an idealized monsoon anticyclone circulation periodically sheds secondary anticyclones due to dynamical instabilities, and observational confirmation of eddy shedding was first shown in Popovic and Plumb (2001). Siu and Bowman (2020) showed that anticyclonic sub-vortices often occur within the AMA at the same time with similar strength. Therefore, consideration of only a single center of the AMA belies the importance of its transient nature and smears out important details.

Recently, Honomichl and Pan (2020) tracked multiple simultaneous maxima of the AMA and identified a third preferred center near 140°E, which is referred to as the western Pacific anticyclone (WPA) or the Bonin high (Enomoto et al., 2003; Enomoto, 2004). Chemical species and low potential vorticity (PV) air within the AMA are shed eastward associated with the emergence of WPA (Vogel et al., 2014; Honomichl & Pan, 2020; Fujiwara et al., 2021). The atmospheric composition and transport pathways associated with the WPA will be systematically investigated in the Asian Summer Monsoon Chemical and Climate Impact Project (ACCLIP) during July-August 2022 (`https://www2.acom.ucar.edu/acclip`).

While observational studies consistently highlight the chemical signature of the WPA, consensus is yet to be reached on the associated dynamics. This topic has a substantial history. For example, Tao and Zhu (1964) pointed out that the AMA moves in the opposite direction of the western Pacific subtropical high at 500 hPa, modulated by the precipitation in east China. Enomoto et al. (2003) used the primitive-equation model in Hoskins and Rodwell (1995) to study the formation mechanism of the (time-averaged) Bonin high. Their model sensitivity analysis showed that the Bonin high disappears by removing the diabatic cooling over the Asian jet while it still exists at monthly timescale when removing the heating in the western Pacific region. Thus, they emphasized the importance of the external Rossby wave source induced by the cooling due to the monsoon-forced descent over the eastern Mediterranean Sea. The wave disturbances along the Asian jet across Eurasia have since been recognized as the “Silk Road (SR) pattern”. In fact, the WPA over Japan was already simulated in Hoskins and Rodwell (1995) but considered to be a model defect after validation against reanalysis data. Further, Enomoto (2004) conducted a composite analysis to study interannual variability of monthly-mean stationary Rossby waves along the subtropical jet (including anticyclonic anomalies over Japan), emphasizing the role of an intensified jet in contributing to the eastward group velocity of stationary waves. Yasui and Watanabe (2010) used dry atmospheric general circulation model and identified the Silk Road pattern as a part the circumglobal teleconnection. They performed a singular value decomposition (SVD) analysis for the diabatic heating and meridional wind anomalies, and concluded that the heating anomalies over the eastern Mediterranean is most responsible for the formation of the WPA, rather than cooling anomalies induced by the monsoon. P. Rupp and Haynes (2021) used a dry dynamical core model to simulate interactions of the Asian monsoon with baroclinic eddies on the westerly jet. They observed a transition from a steady circulation with westward eddy shedding to an unstable eastward eddy shedding state as the background meridional temperature gradient gradually increases. Their results imply that the WPA emerges in response to interaction between localized forcing by monsoon and the mid-latitude baroclinic eddies. Furthermore, Kosaka and Nakamura (2006) aruged that the emergence of the Bonin high can be attributed to the western Pacific convective heating, contradicting the conclusion of Enomoto et al. (2003). The teleconnection between the convective activity in the tropical western Pacific and the upper-level anticyclone anomaly over Japan is called the “Pacific-Japan (PJ) pattern” (Nitta, 1987). R. Lu and Lin (2009) employed a baroclinic model and suggested that the latent heating released from the rainfall anomalies near the Philippine Sea facilitates the eastward wave propagation towards Japan and forms the WPA. Similarly, Ren et al. (2015) showed that the diabatic heating induced by enhanced rainfall over the south China Sea initiates the eastward extension of the AMA. In addition, Kosaka et al. (2009) applied the empirical orthogonal function on monthly-mean 200 hPa meridional winds spanning over the Asian monsoon regions and indicated that the SR pattern and the PJ pattern coincide. Chen and Huang (2012) performed an SVD analysis between upper-level meridional wind across Asia and tropical rainfall on monthly scales and identified that the SR pattern also includes a signature of the PJ pattern. Thus, previous research has concluded that several different mechanisms can contribute to enhancement of the WPA, and our goals include revisiting these mechanisms in the context of transient WPA events. Moreover, the WPA has been mostly examined in the context of monthly and seasonal time scales, but the transient behavior of the WPA associated with eastward eddy shedding has not been fully analyzed.

In this study, we examine the dynamical mechanisms of eastward eddy shedding associated with the formation of WPA, in particular for transient variability. Calculations are based on the latest high resolution reanalysis products from ERA5 (section 2). In section 3, we first analyze the statistical occurrence of enhanced Bonin high events and isolated large amplitude WPA, and their relationships to eastward eddy shedding. Composite patterns of large WPA are analyzed to illustrate the time evolution of shedding events. We define an index to measure the strength of the Bonin high, select isolated large amplitude WPA events, and quantify links with the SR and the PJ patterns, respectively. The dynamics of eastward shedding are then thoroughly investigated with the help of these indices. The goal is to incorporate the synoptic eddy regime into the existing literature. Section 4 concludes the paper.

2 Reanalysis data

We use European Centre for Medium-Range Weather Forecasts (ECMWF) ERA5 meteorological products (Hersbach et al., 2020), including geopotential (z), potential vorticity, zonal and meridional (u and v) wind fields, and temperature. We employ top net thermal radiation (the negative of outgoing longwave radiation, OLR) as a proxy for deep convection. Reanalyses are used at 6-hourly intervals (0000, 0600, 1200, and 1800 UTC) with a horizontal resolution of 0.25° latitude × 0.25° longitude on 37 standard pressure levels. Our investigation focuses on the eastward eddy shedding at 100 hPa during the months of July–August over forty-one years (1979–2019).

3 Results

3.1 Overview of the WPA

Several previous studies of the Asian summer anticyclone identified a single maximum along the geopotential ridge line and found a bimodality behavior, referred to as the Tibetan Plateau (TP) mode and the Iranian Plateau (IP) mode (Q. Zhang et al., 2002; Nützel et al., 2016). Honomichl and Pan (2020) identified multiple simultaneous anticyclonic circulation centers at 100 hPa, and highlighted frequent occurrence of a third center over the western Pacific. We follow their method to identify localized anticyclones, slightly modifying the

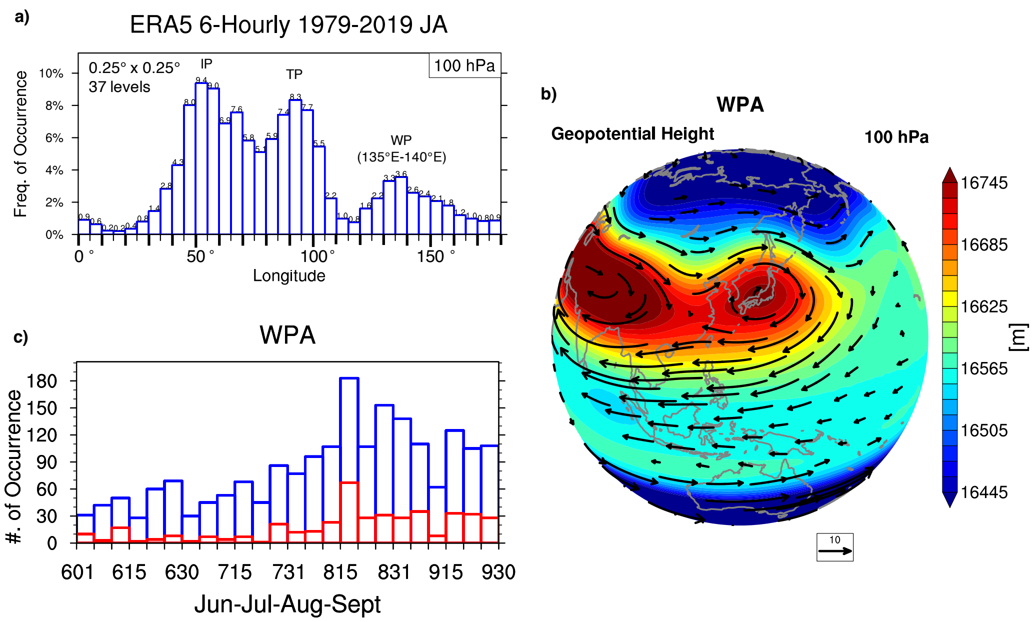

Figure 1. (a) The frequency distribution of the anticyclone centers vs. longitude at 100 hPa compiled using ERA5 6-hourly Geopotential during July-August, 1979-2019 (2542 days in total). Values above each bar indicate the frequency of occurrence in (numbers/2542 days). "IP" refers to the Iranian Plateau mode, "TP" refers to the Tibetan Plateau mode, and "WP" refers to the western Pacific mode. (b) 100 hPa geopotential height (in colors, m) and horizontal circulation (in arrows, m/s) for composites associated with WPA events. (c) The distribution of WPA occurrence dates during June to September of 1979-2019. Blue bars indicate overall histograms while red bars indicate stronger anticyclonic events when the v wind threshold is 6 m/s.

details to eliminate any localized small-scale circulations in the higher resolution ERA5 data. Specifically, maxima are selected only if the meridional wind within 1500 km of the center along the ridge was greater than 3 m/s (-3 m/s) on the west (east) side. Note that we have adopted a more strict criterion (3 m/s vs. 0 m/s threshold as in Honomichl & Pan, 2020) for selecting local maxima due to the finer horizontal grid resolution of ERA5 than ERA-Interim. Fig. 1a shows the histogram of frequency and longitude of transient anticyclone centers at 100 hPa for July–August. In addition to the IP mode near 50°E and TP mode near 90°E, a third preferred center is found over the western Pacific (WP) peaking around 135°-140°E. The frequency distribution is almost identical to the previously calculated result (Fig. 3a, Honomichl & Pan, 2020), and similar to the results of Siu and Bowman (2020). We've repeated the analysis on meteorological fields at 150 hPa level and found that the locations for the WPA remain the same (not shown).

To gain a better understanding of the dynamical processes leading to the eastward eddy shedding, we define the WPA event as anticyclonic center that falls within the 135°-140°E longitudinal bin during July-August. This analysis selects 614 samples using 6-hourly data over 41 years and construct 100 hPa geopotential composite; these 614 samples represent $\sim$ 140 seperate events during 1979-2019, i.e. typically 3-4 events per year. As displayed in Fig. 1b, a localized maximum of geopotential and associated meridional winds identifies a separate anticyclone is prominent in the western Pacific region, adjacent to the AMA. Figure 1c shows the number of WPA events during June to September during 1979-2019, suggesting that the occurrence of WPA peaks in late August and drops in September. Sensitivity test shows that doubling the v wind criterion to 6 m/s, i.e., selecting stronger localized anticyclones, doesn't change the shape of the distribution as indicated by red bars. We note that the distribution of anticyclonic centers for June-September is similar to that in Fig. 1a (not shown), and the composited signals are about the same as for July-August.

To quantify the strength of the anticyclone over Japan, a Bonin high Index (BHI) is defined as the regional averaged geopotential height within 30°-55°N and 135°-140°E. Figure 2 shows time series of the BHI during July and August 1979-2019, along with identified WPA events. The curves exhibit substantial intraseasonal and yearly variabilities in frequency and intensity. Overall, the WPA events typically coincide well with peaks in BHI, although not for all events. It is because we require the WPA to be an anticyclonic cell while the BHI does not indicate a closed contour, e.g., a strong ridge can create large BHI but not WPA.

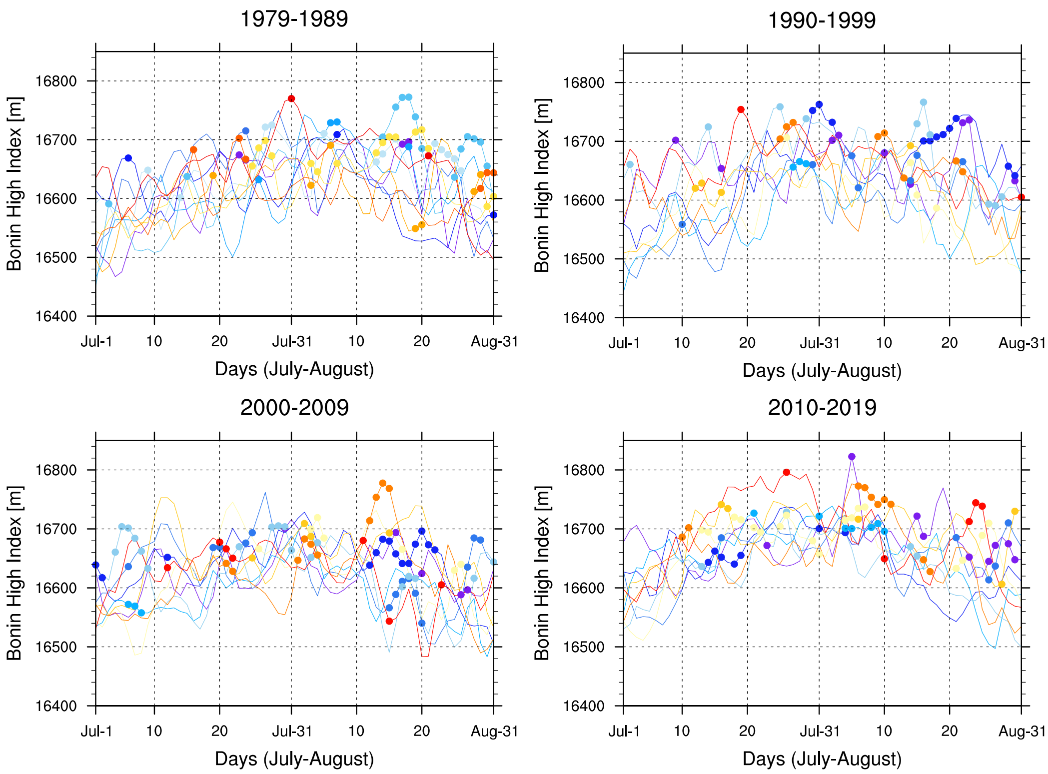

Figure 2. The color curves show the time series of the BHI in July-August over 41 years. Each color curve represent one year. Colored dots indicate the identified WPA events.

The 100 hPa geopotential and meridional wind anomalies composited for the WPA events are shown in Fig. 3a and b, respectively. We subtract the climatological mean value for each time step to derive a deseasonalized anomaly. Here Day 0 denotes the day the WPA event occurs. The composited wave packet structure shows disturbances embedded along the climatological westerly flow with an approximate zonal scale of wavenumber 6. Positive geopotential coupled with intensified anticyclone occurs near the jet exit above Japan. The composite features are not sensitive to the choice of the longitude range in defining the WPA events (not shown). Time development of geopotential height averaged over 40°-45°N along the upper-level jet at 100 hPa is depicted by the Hovmöller diagram in Fig. 3c, highlighting coherent upstream wave structure beginning ~ 4 days prior to the WPA events. The wave packet has near zero phase velocity, but a clear eastward group velocity near 24 m/s. The wave packet propagates downstream through the waveguide of the jet core, and amplifies near the jet exit on Day 0. The quasi-stationary zonal wavenumber 6 structure identified in Fig. 3 is consistent with the SR behavior analyzed in Kosaka et al. (2009), interpreted as a stationary Rossby wave on the background westerly jet. During Day +1 to +4, wave packets develop successively downstream and reach the Pacific coast of the United States.

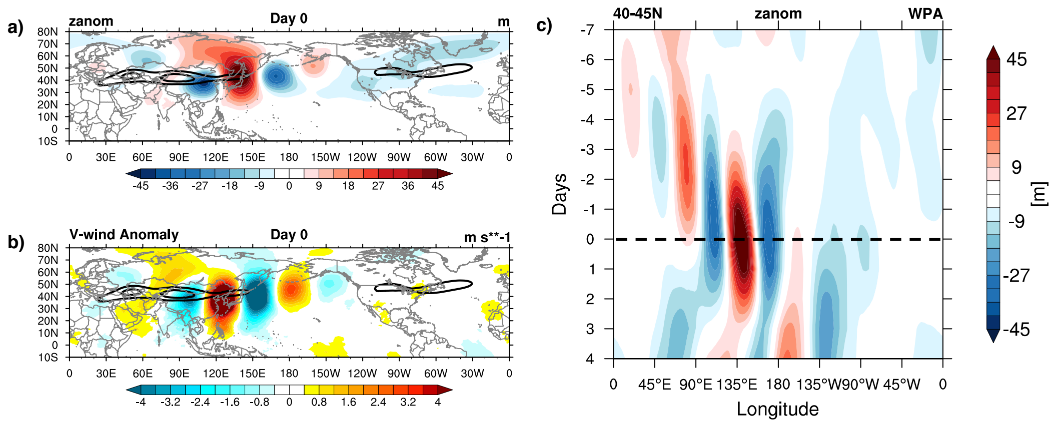

Figure 3. Composites of 100 hPa geopotential and meridional wind anomalies (zanom and vanom) for the WPA events on Day 0 in (a) and (b), respectively. Regions where anomalies are not significant at the 95% level using t-test are shaded white. Black contours highlight the 200 hPa climatological westerly jet of 24 and 30 m/s. (c) Hovmöller diagram of zanom at 100 hPa averaged over 40°-45°N from Day -7 to +4.

Fig. 4a displays the time evolution of PV interpolated to 360 K isentrope for the composited WPA events. The anticyclone is associated with a region of relatively low PV,

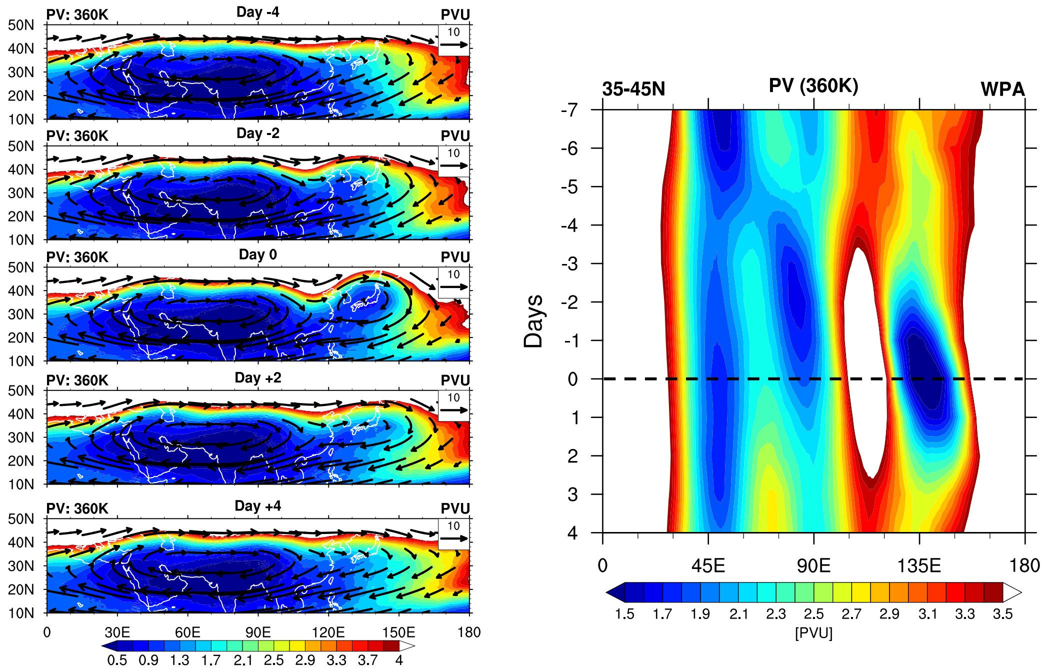

Figure 4. (a) Composite patterns of PV (in colors, PVU) at 360 K overlaid with the winds at 100 hPa (in vectors, m/s) on Day -4, Day -2, Day 0, Day +2, and Day +4 of the WPA events, respectively. (b) Hovmöller diagram of PV at 360 K averaged over 35°-45°N from Day -7 to Day +4.

e.g. Garny and Randel (2016) and Ploeger et al. (2017). Low PV patches develop on the eastern side of the anticyclone during the WPA events, in a manner consistent with wave trains seen in Fig. 3. Fig. 4b shows a Hovmöller diagram of PV at 360 K averaged over 35°-45°N from Day -7 to +4, highlighting development of low PV air over the composite WPA life cycle. During Day -4 to +2, the low PV air associated with the eastward shedding is confined between 120°-150°E and remains quasi-stationary, consistent with the geopotential signature in Fig. 3. The PV evolution is consistent with the developing WPA transporting air masses with elevated mixing ratios of CO and H_2O rapidly into the extratropical lower stratosphere (Ploeger et al., 2015; Pan et al., 2016). We note that while the WPA is quasi-stationary, air parcel trajectories can move through the circulation and transport constituents towards the east, e.g. Honomichl and Pan (2020), their Fig. 7.

The composited WPA meteorological features include combined effects of the SR and PJ teleconnections – wave trains in the upper troposphere together with enhanced convection over the tropical western Pacific (Fig. S1). However, the SR and PJ patterns do not always coincide in individual cases, which motivates us to evaluate the WPA events in terms of relations to the SR and PJ indices and examine their dynamics separately.

3.2 WPA Relationships to the Silk Road Pattern

3.2.1 Defining a Silk Road Index

The most striking feature in Fig. 3 is the quasi-stationary wave along the upper-level jet, resembling the SR pattern (R.-Y. Lu et al., 2002; Enomoto et al., 2003). To quantify the occurrence of the Silk Road wave trains, we construct a time varying Silk Road Index (SRI). As indicated by the composite map of geopotential height averaged over Day -4 to -1 preceding the WPA events in Fig. 5, we see that the SR pattern consists of four zonally oriented anomaly centers confined to 35°-55°N, located over **A** the Caspian Sea (40°-55°E), **B** central Asia (70°-85°E), **C** Mongolia (95°-115°E), and **D** east China (120°-140°E). Two negative geopotential centers are marked as **A** and **C** while two positive centers are marked as **B** and **D**. We define za_i as the maximum anomaly value in each box and SRI is the sum of absolute values of the four boxes as in Eq. 1:

$$SRI = \sum_{i=A,C} -za_i + \sum_{i=B,D} za_i \tag{1}$$

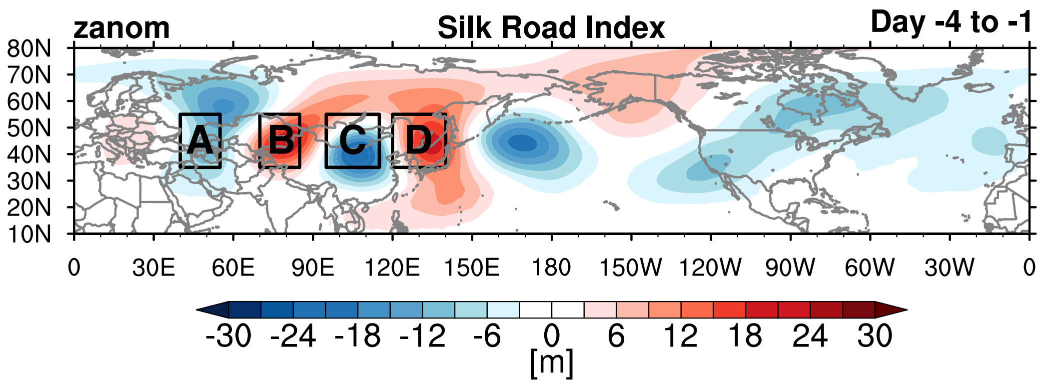

Figure 5. Schematic illustrating four centers where the SRI is constructed. The zanom composites (in colors) are averaged during Day -4 to -1 prior to the WPA events.

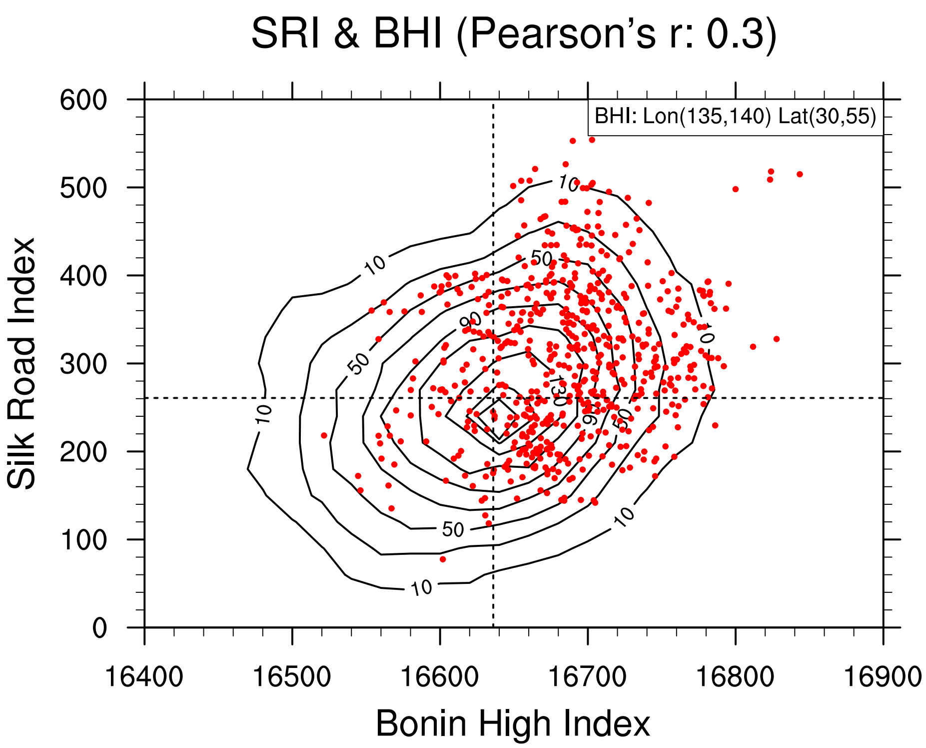

Figure 6. Two dimensional distribution of the SRI against the BHI compiled using all July-August data during 1979-2019. Red dots indicate the WPA events. Dashed reference lines indicate the median values. Correlation coefficient is given in the figure title.

Figure 6 shows a 2D distribution of SRI vs. BHI for all daily samples over July-August 1979-2019. Contours represent the density of scatter points. There is a weak but statistically significant correlation in the distribution (r $\sim$ 0.3), as expected from the results in Fig. 3. The red dots in Fig. 6 represent the WPA events, primarily falling in the upper right-hand quadrant, i.e. large amplitude BHI and SRI. These statistics are consistent with an amplified Silk Road pattern typically preceding the strong anticyclone above Japan by 1 to 4 days.

3.2.2 Dynamics in Relation to the Silk-Road Pattern

We apply composite analysis to obtain the essential circulation patterns of the WPA with reference to the intensity of the SR pattern. To sharpen the composited features, variables whose SRI fall above the 75^{th} percentile are selected. Wave activity flux (WAF) vectors are computed to identify the origin and propagation of Rossby waves associated with the WPA events coinciding with the pronounced SR pattern. The calculation is based on the methods of Takaya and Nakamura (2001), which generalizes Plumb fluxes (Plumb, 1979) to allow for transient eddies propagating in a zonally varying mean state. The WAF is designed in the quasi-geostrophic (QG) framework, whose direction is parallel to the wave group velocity and the divergence (convergence) implies source (sink) of Rossby waves (H.-H. Hsu & Lin, 2007; Gu et al., 2018).

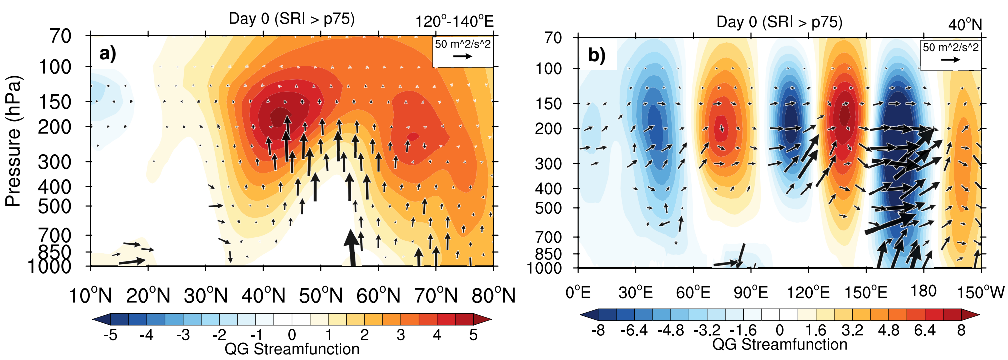

Figure 7. Cross sections of QG streamfunction anomalies (in colors, unit: $10^{-6}m^2/s$) and WAF (in vectors, unit: m^2/s^2) (a) averaged over 120°-140°E and (b) at 40°N composited for the WPA events which coincide with pronounced Silk Road pattern.

Figure 7a shows a latitude–height cross-section of QG streamfunction anomalies and WAF averaged over 120°-140°E. Positive anomalous streamfunction around 150 hPa is equivalent to enhanced geopotential height fields, accompanying the upward flux from the lower troposphere near 40°-50°N above Japan, which is indicative of poleward eddy heat flux. Fig. 7b is the meridional section at 40°N, highlighting a train of high/low geopotential height anomaly centers in the upper troposphere with eastward-pointing WAF. This behavior is consistent with the eastward group velocity seen in Fig. 3c.

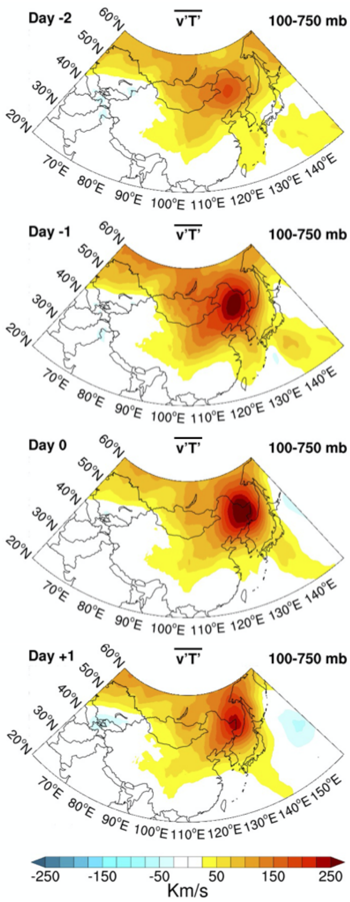

Figure 8. The vertically-averaged eddy heat flux ($\overline{v'T'}$, Km/s) during Day -2 to +1 of the WPA events.

The quasi-stationary zonal wavenumber 6 structure of the WPA/SR wave train is consistent with calculated stationary Rossby waves on the background westerly jet, which acts as a waveguide (Ding & Wang, 2005; Kosaka et al., 2009). The preferential phase locking of large WPA events, where the anticyclonic eddy maximum anchors near 135°-140°E rather than randomly moving around, may be related to the downstream end of the jet near these longitudes (Fig. 3a). Geographically fixed anomaly patterns along a localized baroclinic jet have been discussed in Hoskins and Ambrizzi (1993), Ambrizzi et al. (1995), and H.-H. Hsu and Lin (1992). Background localized jet structure can also lead to amplification or over-reflection near the jet exit (Branstator, 1983; Hoskins & Ambrizzi, 1993), where the meridional gradient of absolute vorticity is close to zero (R. S. Lindzen & Tung, 1978). Calculations show that the meridional gradient of absolute vorticity at the jet exit is close to zero in 41-year climatology and also during the WPA events (not shown), supporting the possibility of wave over-reflection.

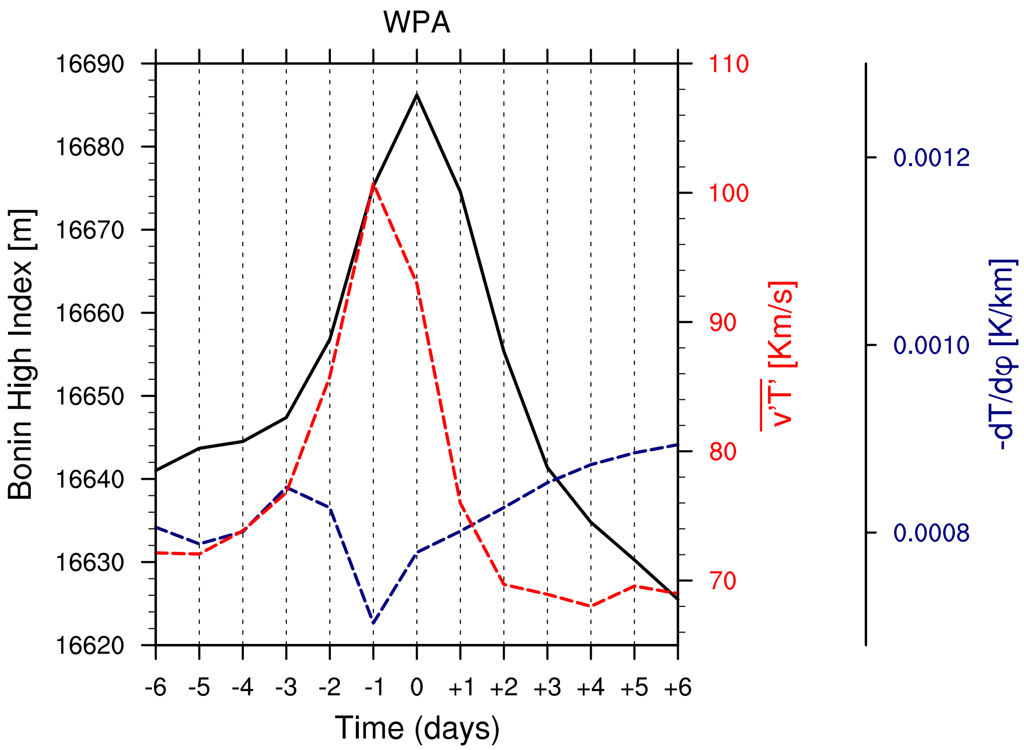

Figure 9. Life cycles of the composited WPA events in terms of BHI (solid black line), the vertically-integrated heat flux averaged over 90°-130°E and 30°-60°N (dashed red line), and the background meridional temperature gradient averaged over 115°-130°E and 30°-40°N (dashed navy line) during Day -6 to +6 of the WPA events.

The wave activity fluxes in Fig. 7a suggest close relationship with eddy heat fluxes ($\overline{v'T'}$), signifying baroclinic wave growth. We further show the evolution of the vertically-averaged eddy heat fluxes from 750 to 100 hPa in Figure 8. From Day -2 to -1, the northward eddy heat transport exhibits a strong local maximum over 90°-130°E and 30°-60°N slightly upstream of the WPA, suggesting an active role in amplifying the geopotential height anomaly downstream on Day 0. The heat fluxes gradually weaken and move northeastward on Day +1. The relationship to the composite WPA is quantified in Fig. 9, showing a life cycle of BHI amplification lasting several days (c.f. Fig. 3c). Time variations in WPA composite $\overline{v'T'}$ shows a strong peak one day prior to the BHI maximum. The peak in baroclinic growth preceding the wave amplitude maximum is a signature of baroclinic forcing for the WPA events, and this behavior is similar to life cycles of idealized wavenumber-6 Rossby waves (Edmon Jr et al., 1980) and observations in the South Hemisphere (Randel & Stanford, 1985). In addition, we observe systematic changes in background temperature gradient ($-\frac{\partial T}{\partial \phi}$, see Fig. S2) over 115°-130°E and 30°-40°N from Day -3 to -1. This behavior is a clear signature of baroclinic wave growth, associated with heat transport down the mean temperature gradient and remove available potential energy from the mean flow. In Fig. 9, the dashed navy line shows weakening of $-\frac{\partial T}{\partial \phi}$ in association with baroclinic wave development. These results are also consistent with the findings of P. Rupp and Haynes (2021), who show that baroclinic eddies are intensified due to interaction with the northern edge of the anticyclone (see their Fig 14c and 16).

3.3 WPA Relationships to the Pacific-Japan Pattern

3.3.1 Defining a Pacific-Japan Index

Composited OLR anomaly patterns for WPA events reveal that enhanced convection occurs over the tropical western Pacific several days prior to the WPA events (Fig. S1), which has been confirmed by the composites of precipitation anomalies (not shown). However, we find that this pattern is largely dominated by a few extreme events. As shown in Fig. 10, the OLR anomalies in the vicinity of the Philippines and the South China Sea (10°-30°N, 130°-160°E) differ widely when the averaged OLR anomaly during day -6 to day -2 is below (Fig. 10a) and above (Fig. 10b) the 25^{th} percentile of all WPA events. Fig. 10a displays a north-south tripolar pattern, characterized by zonally elongated anomalies with signs changing alternatively from 0°-45°N along the eastern Pacific, signifying enhanced convective activity near 20N sandwiched between two suppressed convection centers. This meridional teleconnection is referred to as the PJ pattern (Nitta, 1987; Kosaka & Nakamura, 2006; H.-H. Hsu & Lin, 2007; Kosaka et al., 2009; Kosaka & Nakamura, 2010). However, the relation of OLR to WPA events disappears in composites for the lower 75% fraction (Fig.

10b). This distinct contrast between Fig. 10a and 10b demonstrates that a small fraction of the WPA events are associated with the PJ pattern while most of the cases aren't.

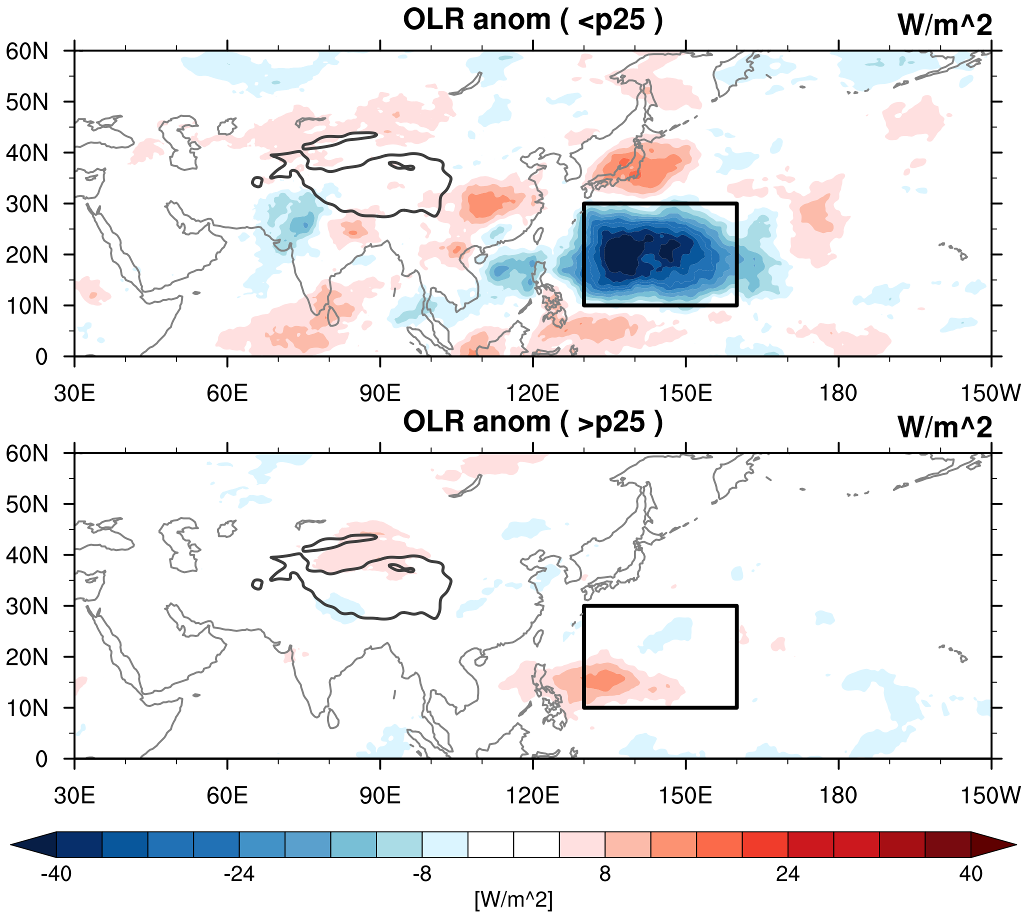

Figure 10. The composite maps of OLR anomalies (W/m^2) during Day -6 to Day -2 prior to the WPA events, separated according to the regional average over the boxed region (10°-30°N and 130°-160°E) falls (a) below and (b) above the 25^{th} percentile. Black contours delineate the topographic boundary of 3000 m.

The (negative) OLR anomaly averaged in the boxed region in Fig. 10 during day -6 to -2 prior to the WPA events is used as the Pacific-Japan Index (PJI) – the stronger convection around Philippines and the South China Sea, the lower OLR anomaly, and the larger PJI value. Fig. 11a shows that the scatterplot between the PJI against BHI for the identified WPA events. Overall, there is weak correlation (0.27*, where asterisk denotes statistical significance at the 95% confidence level), although there is stronger relationship for extreme PJ patterns. For instance, red dots represent the WPA events whose PJI falls above the 75^{th} percentile and suggest a positive correlation with the intensity of the WPA. Figure 11b shows only the *significant* correlation coefficients between the PJI and the BHI as the PJI increases from -30, -20, ..., 20, 30 W/m^2. The correlation is in fact maximized when the PJI falls above the upper 30^{th} percentile (0.47*) while becomes insignificant as the PJI reaches 20 W/m^2. The upper 30^{th} percentile agrees well with statistics of back trajectories initialized within the WPA in Honomichl and Pan (2020), where one third of air parcels trace back to the Philippine Sea.

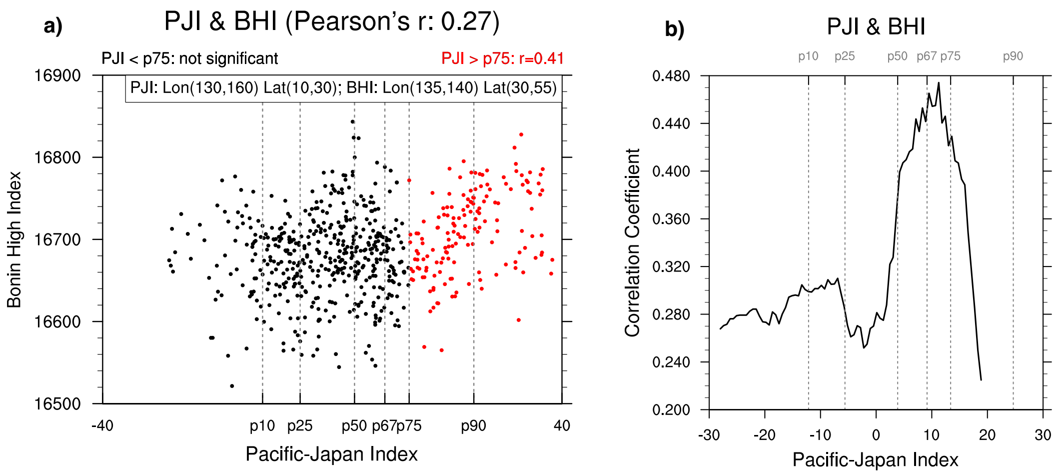

Figure 11. (a) Scatterplot between the BHI (m) against the PJI (W/m^2) composited for a total of 614 Bonin high events. Red dots highlight the Bonin high events whose PJI falls above the 75^{th} percentile. Correlation coefficients are given in the figure title. Gray reference lines indicate the 10^{th} (p10), the 25^{th} (p25), the median (p50), the 67^{th} (p67), the 75^{th} (p75), and the 90^{th} (p90) percentiles of the PJI, respectively. (b) Curve indicates the *significant* correlation between subsets of the BHI and PJI, which are regrouped as the PJI increases.

3.3.2 Dynamics in Relation to the Pacific-Japan Pattern

We apply composite analysis to identify the circulation patterns with reference to the intensity of the PJ pattern. Similar to Section 3.2.2, variables composited for the WPA events on Day 0 are averaged when the corresponding PJI falls above the 75^{th} percentile, i.e. enhanced convection as in Fig. 10a (represented by gray contours in Fig. 12b). Fig. 12a shows the latitude-height cross section of QG streamfunction anomalies with WAF vectors averaged over 120°-140°E. We see enhanced convection near the Philippine sea in accordance with negative zanom, triggering wave trains that propagate upward and poleward. Figure 12b exhibits that wave trains at 850 hPa originate from south of Japan and reach the Gulf of Alaska roughly along an arc route, agreeing well with findings in previous studies (Fig. 4 in R. Lu, 2004; Kosaka & Nakamura, 2006, 2010). Hoskins and Karoly (1981) provided an explanation for the great circle–like wave path using a baroclinic model. They've found that Rossby wave energy dispersion theory can describe the atmospheric activity at varying latitudes in a spherical atmosphere. The perturbation around 15°N initially moved northeastward, and then longer waves ($K_s \leq 3$) continued to propagate poleward while shorter waves were trapped by the northern flank of the jet and turned southeastward. According to the ray tracing method (Eq. 5.27 in Hoskins & Karoly, 1981), the turning latitude for tropical wavenumber 6 locates at around 45°N, consistent with the anomaly patterns shown in Fig. 12b.

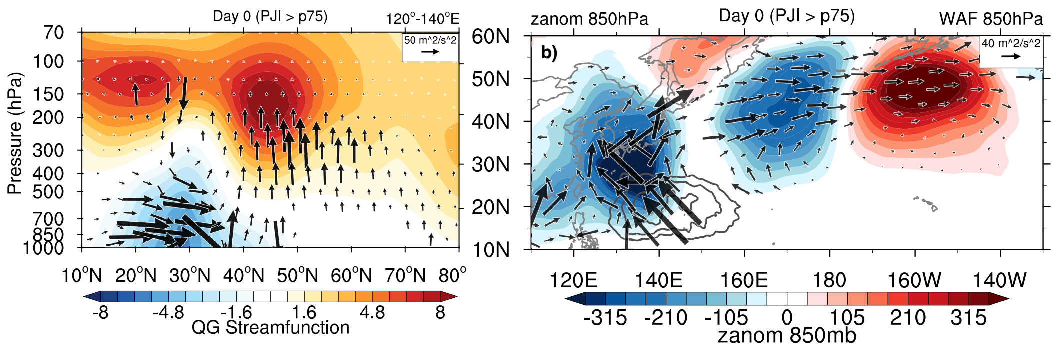

Figure 12. (a) Cross section of QG streamfunction anomalies (in colors, unit: $10^{-6}m^2/s$) and WAF (in vectors, unit: m^2/s^2) averaged over 120°-140°E. (b) 850 hPa composited geopotential anomalies (in colors) together with WAFs (in vectors, unit: m^2/s^2) for the WPA events coinciding with the pronounced PJ pattern. Gray contours represent negative OLR anomaly center (-50, -40, -30, ... in W/m^2) as in Fig. 10a.

4 Discussion and Conclusion

The Asian monsoon anticyclone exhibits a large spatial and temporal variability on the subseasonal scale. Using long-term ERA5 6-hourly reanalysis products, we have confirmed that the AMA forms a trimodal distribution in longitudes near 50°E (IP mode), 90°E (TP mode), and 135°E (WP mode) during July and August (Honomichl & Pan, 2020). The WP mode is accompanied by transient eddies that amplify as part of quasi-stationary wave trains, leading to a closed anticyclone over the Western Pacific with isolated low PV air. The frequency of the WPA occurrence peaks in late August. This work has focused on the dynamics driving the eastward eddy shedding associated with the presence of the WPA on synoptic time scales. While composited anomaly fields show combined influence of the SR and PJ patterns, these two teleconnections do not always coincide during the development of individual cases. Therefore, we categorized the WPA events into ones related to the SR and PJ mechanisms, respectively, and defined indices to quantify their features accordingly.

First, the BHI is significantly correlated with the SRI, demonstrating that WPA events are closely tied with pronounced Silk Road wave trains. The WPA amplitude growth is closely linked with systematic fluctuations in baroclinic wave forcing linked with eddy heat fluxes. The SR-related WPA reaches its largest amplitude one day after its maximum baroclinic growth, indicating anticyclonic eddies grow along the jet in response to the strong baroclinic background. We also find consistent relaxation of the background temperature gradient throughout the WPA life cycles (Fig. 9). These results are consistent with the model simulations reported by P. Rupp and Haynes (2021), in which they found that baroclinic eddies grow on the northern edge of the anticyclone with strong meridional temperature gradient. We furthermore estimated the seasonal cycle of the maximum growth rate of baroclinic instabilities given by R. Lindzen and Farrell (1980): $0.31\frac{g}{a\bar{T}N}|-\frac{\partial\bar{T}}{\partial\phi}|$, with $\bar{T}$ the temperature averaged from 100 hPa to 750 hPa; a the Earth's radius; g the gravity acceleration; and N the Brunt-Väisälä frequency (not shown). The baroclinic instability along the mid-latitude belt (30°-60°N, 0°-180°E) grows as the season progresses with correspondingly more WPA events in August (see Fig. 1c), contributing to the seasonal variation in the WPA occurrence. While our results show clear links to dynamical structure, we do not find coherent changes in convective activity over the Bay of Bengal, the Tibetan Plateau and southern China prior to WPA growth (see Fig. S1), implying that the eddies are not linked with convective forcings over the Indian summer monsoon region but rather with internal jet dynamics (Sato & Takahashi, 2006; Song et al., 2013; Amemiya & Sato, 2020). Although not shown, we've confirmed this finding by performing lag correlation between the BHI and multiple Indian summer monsoon indices (B. Wang & Fan, 1999), specifically, one convection index that characterizes the intensity change of the convective heating over the Bay of Bengal, as well as three circulation indices that quantify the Indian monsoon driven baroclinicity and the strength of the monsoon Hadley circulation over the Indian subcontinent. No significant correlation with the BHI can be identified among these indices based on the tropics from day -10 to 0, suggesting the limited role of monsoon dynamics in exciting SR-related baroclinic eddies.

Second, the correlation between the BHI and PJI suggests that about one third of the WPA events are associated with the PJ pattern. Composite analyses for the PJ-related WPA events show that perturbations originate in the lower troposphere due to convective forcing, radiating upward and maximizing in the UTLS region. Convective activities shift progressively northeastward from the Bay of Bengal to the western North Pacific from July to August (Fig. 8 in B. Wang & Fan, 1999). The wet season peaks in late July over the northern Philippine and in August over the Philippine Sea (B. Wang, 1994). Meanwhile, typhoon activity peaks in August on the east of the Philippines (L. Wu et al., 2014), resulting in more excitation of the PJ pattern (Kawamura & Ogasawara, 2006; Yamada & Kawamura, 2007). Consistent with this behavior, observations show that 70% of the PJ-related WPA events occur in August.

Previous studies have shown the monthly SR pattern coexists with the PJ pattern (Kosaka et al., 2009; Chen & Huang, 2012). Here, we've found that the SRI is not significantly correlated with the PJI (not shown), suggesting that the SR and PJ mechanisms are physically independent processes. The two patterns coincide as a consequence of chance occurrence – enhanced convection in the tropical western Pacific at the right time a Silk Road wave train is traveling along. The monthly resolution used in previous studies is too coarse for differentiating the two processes. This is consistent with results in Sato and Takahashi (2006) that although the regression analysis show the Silk Road wave is correlated with the stronger convective activity over the western Pacific, the divergent wind caused by the convection cannot excite the eastward propagating stationary Rossby wave coming from the upstream.

Overall, our results indicate that the transient eastward shedding associated with the WPA is primarily related to the Silk Road pattern. Eddies develop eastward in a baroclinically unstable background along the midlatitude westerlies, interact with the AMA with low PV and high pollutants, split the monsoon anticyclone into isolated parts, and redistribute the air to the preferred location of the WPA. Meanwhile, about one third of the WPA are substantially influenced by Philippines convection through the Pacific-Japan mechanism.

Anticyclonic eddies propagate upward and disperse eastward along the great circle as a consequence of strong rainfall and typhoons in the vicinity of the Philippines, especially active in August. The two mechanisms are not significantly and physically correlated on synoptic scales. More WPA events occur in August as a result of a combination of strong baroclinic instability on the northern edge of the AMA and the intensified Philippines convection. This work has synthesized previous studies and provided insights from dynamical perspectives for the design and implementation of the ACCLIP campaign.

Acknowledgments

We thank several colleagues for discussions during the course of this work, including Shawn Honomichl, Warren Smith, Peter Haynes, Philip Rupp, and Na Wang. The authors appreciate the constructive discussion with the UTLS Group at the Atmospheric Chemistry Observations and Modeling, NCAR. We also acknowledge high-performance computing support from Brown Community Cluster provided by Purdue University. Xinyue Wang is supported by the NSF via the NCAR's Advanced Study Program Postdoctoral Fellowship.

References

Ambrizzi, T., Hoskins, B. J., & Hsu, H.-H. (1995). Rossby wave propagation and teleconnection patterns in the austral winter. *Journal of Atmospheric Sciences*, *52*(21), 3661–3672.

Amemiya, A., & Sato, K. (2020). Characterizing quasi-biweekly variability of the Asian monsoon anticyclone using potential vorticity and large-scale geopotential height field. *Atmospheric Chemistry and Physics*, *20*(22), 13857–13876.

Branstator, G. (1983). Horizontal energy propagation in a barotropic atmosphere with meridional and zonal structure. *Journal of Atmospheric Sciences*, *40*(7), 1689–1708.

Chen, G., & Huang, R. (2012). Excitation mechanisms of the teleconnection patterns affecting the July precipitation in northwest China. *Journal of Climate*, *25*(22), 7834–7851.

Ding, Q., & Wang, B. (2005). Circumglobal teleconnection in the northern hemisphere summer. *Journal of climate*, *18*(17), 3483–3505.

Edmon Jr, H., Hoskins, B., & McIntyre, M. (1980). Eliassen-Palm cross sections for the troposphere. *Journal of Atmospheric Sciences*, *37*(12), 2600–2616.

Enomoto, T. (2004). Interannual variability of the Bonin high associated with the propagation of Rossby waves along the Asian jet. *Journal of the Meteorological Society of Japan. Ser. II*, *82*(4), 1019–1034.

Enomoto, T., Hoskins, B. J., & Matsuda, Y. (2003). The formation mechanism of the Bonin high in August. *Quarterly Journal of the Royal Meteorological Society: A journal of the atmospheric sciences, applied meteorology and physical oceanography*, *129*(587), 157–178.

Fujiwara, M., Sakai, T., Nagai, T., Shiraishi, K., Inai, Y., Khaykin, S., … Pan, L. L. (2021). Lower-stratospheric aerosol measurements in eastward-shedding vortices over japan from the asian summer monsoon anticyclone during the summer of 2018. *Atmospheric Chemistry and Physics*, *21*(4), 3073–3090.

Garny, H., & Randel, W. (2013). Dynamic variability of the Asian monsoon anticyclone observed in potential vorticity and correlations with tracer distributions. *Journal of Geophysical Research: Atmospheres*, *118*(24), 13–421.

Garny, H., & Randel, W. J. (2016). Transport pathways from the Asian monsoon anticyclone to the stratosphere. *Atmospheric Chemistry and Physics*, *16*(4), 2703–2718.

Gu, S., Zhang, Y., Wu, Q., & Yang, X.-Q. (2018). The linkage between arctic sea ice and midlatitude weather: In the perspective of energy. *Journal of Geophysical Research: Atmospheres*, *123*(20), 11–536.

Hersbach, H., Bell, B., Berrisford, P., Hirahara, S., Horányi, A., Muñoz-Sabater, J., … others (2020). The ERA5 global reanalysis. *Quarterly Journal of the Royal Meteorological Society*, *146*(730), 1999–2049.

Honomichl, S. B., & Pan, L. L. (2020). Transport from the asian summer monsoon anticyclone over the western pacific. *Journal of Geophysical Research: Atmospheres*, *125*(13), e2019JD032094.

Höpfner, M., Ungermann, J., Borrmann, S., Wagner, R., Spang, R., Riese, M., … others (2019). Ammonium nitrate particles formed in upper troposphere from ground ammonia sources during Asian monsoons. *Nature geoscience*, *12*(8), 608–612.

Hoskins, B. J., & Ambrizzi, T. (1993). Rossby wave propagation on a realistic longitudinally varying flow. *Journal of Atmospheric Sciences*, *50*(12), 1661–1671.

Hoskins, B. J., & Karoly, D. J. (1981). The steady linear response of a spherical atmosphere to thermal and orographic forcing. *Journal of Atmospheric Sciences*, *38*(6), 1179–1196.

Hoskins, B. J., & Rodwell, M. J. (1995). A model of the Asian summer monsoon. Part I:

The global scale. *Journal of the Atmospheric Sciences*, *52*(9), 1329–1340.

Hsu, C. J., & Plumb, R. A. (2000). Nonaxisymmetric thermally driven circulations and upper-tropospheric monsoon dynamics. *Journal of the atmospheric sciences*, *57*(9), 1255–1276.

Hsu, H.-H., & Lin, S.-H. (1992). Global teleconnections in the 250-mb streamfunction field during the northern hemisphere winter. *Monthly weather review*, *120*(7), 1169–1190.

Hsu, H.-H., & Lin, S.-M. (2007). Asymmetry of the tripole rainfall pattern during the east asian summer. *Journal of Climate*, *20*(17), 4443–4458.

Kawamura, R., & Ogasawara, T. (2006). On the role of typhoons in generating PJ teleconnection patterns over the western North Pacific in late summer. *Sola*, *2*, 37–40.

Kosaka, Y., & Nakamura, H. (2006). Structure and dynamics of the summertime Pacific–Japan teleconnection pattern. *Quarterly Journal of the Royal Meteorological Society: A journal of the atmospheric sciences, applied meteorology and physical oceanography*, *132*(619), 2009–2030.

Kosaka, Y., & Nakamura, H. (2010). Mechanisms of meridional teleconnection observed between a summer monsoon system and a subtropical anticyclone. Part I: The Pacific–Japan pattern. *Journal of Climate*, *23*(19), 5085–5108.

Kosaka, Y., Nakamura, H., Watanabe, M., & Kimoto, M. (2009). Analysis on the dynamics of a wave-like teleconnection pattern along the summertime Asian jet based on a reanalysis dataset and climate model simulations. *Journal of the Meteorological Society of Japan. Ser. II*, *87*(3), 561–580.

Lindzen, R., & Farrell, B. (1980). A simple approximate result for the maximum growth rate of baroclinic instabilities. *Journal of the atmospheric sciences*, *37*(7), 1648–1654.

Lindzen, R. S., & Tung, K. (1978). Wave overreflection and shear instability. *Journal of Atmospheric Sciences*, *35*(9), 1626–1632.

Liu, Y., Hoskins, B., & Blackburn, M. (2007). Impact of Tibetan orography and heating on the summer flow over Asia. *Journal of the Meteorological Society of Japan. Ser. II*, *85*, 1–19.

Lu, R. (2004). Associations among the components of the east asian summer monsoon system in the meridional direction. *Journal of the Meteorological Society of Japan. Ser. II*, *82*(1), 155–165.

Lu, R., & Lin, Z. (2009). Role of subtropical precipitation anomalies in maintaining the summertime meridional teleconnection over the western north pacific and east asia.

Journal of Climate, *22*(8), 2058–2072.

Lu, R.-Y., Oh, J.-H., & Kim, B.-J. (2002). A teleconnection pattern in upper-level meridional wind over the North African and Eurasian continent in summer. *Tellus A: Dynamic Meteorology and Oceanography*, *54*(1), 44–55.

Manney, G. L., Santee, M. L., Lawrence, Z. D., Wargan, K., & Schwartz, M. J. (2021). A Moments View of Climatology and Variability of the Asian Summer Monsoon Anticyclone. *Journal of Climate*, *34*(19), 7821–7841.

Nitta, T. (1987). Convective activities in the tropical western Pacific and their impact on the Northern Hemisphere summer circulation. *Journal of the Meteorological Society of Japan. Ser. II*, *65*(3), 373–390.

Nützel, M., Dameris, M., & Garny, H. (2016). Movement, drivers and bimodality of the South Asian High. *Atmospheric Chemistry and Physics*(16), 14755–14774.

Pan, L. L., Honomichl, S. B., Kinnison, D. E., Abalos, M., Randel, W. J., Bergman, J. W., & Bian, J. (2016). Transport of chemical tracers from the boundary layer to stratosphere associated with the dynamics of the Asian summer monsoon. *Journal of Geophysical Research: Atmospheres*, *121*(23).

Ploeger, F., Gottschling, C., Griessbach, S., Grooß, J.-U., Guenther, G., Konopka, P., ... others (2015). A potential vorticity-based determination of the transport barrier in the Asian summer monsoon anticyclone. *Atmospheric chemistry and physics*, *15*(22), 13145–13159.

Ploeger, F., Konopka, P., Walker, K., & Riese, M. (2017). Quantifying pollution transport from the Asian monsoon anticyclone into the lower stratosphere. *Atmospheric Chemistry and Physics*, *17*(11), 7055.

Plumb, R. (1979). Eddy fluxes of conserved quantities by small-amplitude waves. *Journal of atmospheric sciences*, *36*(9), 1699–1704.

Popovic, J. M., & Plumb, R. A. (2001). Eddy shedding from the upper-tropospheric Asian monsoon anticyclone. *Journal of the atmospheric sciences*, *58*(1), 93–104.

Randel, W. J., & Park, M. (2006). Deep convective influence on the Asian summer monsoon anticyclone and associated tracer variability observed with Atmospheric Infrared Sounder (AIRS). *Journal of Geophysical Research: Atmospheres*, *111*(D12).

Randel, W. J., Park, M., Emmons, L., Kinnison, D., Bernath, P., Walker, K. A., ... Pumphrey, H. (2010). Asian monsoon transport of pollution to the stratosphere. *Science*, *328*(5978), 611–613.

Randel, W. J., & Stanford, J. L. (1985). The observed life cycle of a baroclinic instability. *Journal of Atmospheric Sciences*, *42*(13), 1364–1373.

Randel, W. J., Zhang, K., & Fu, R. (2015). What controls stratospheric water vapor in the NH summer monsoon regions? *Journal of Geophysical Research: Atmospheres*, *120*(15), 7988–8001.

Ren, X., Yang, D., & Yang, X.-Q. (2015). Characteristics and mechanisms of the subseasonal eastward extension of the south asian high. *Journal of Climate*, *28*(17), 6799–6822.

Rupp, P., & Haynes, P. (2021). Zonal scale and temporal variability of the Asian monsoon anticyclone in an idealised numerical model. *Weather and Climate Dynamics Discussions*, 1–31.

Rupp, P. M., & Haynes, P. H. (2020). Spatio-temporal stability analysis applied to monsoon anticyclone flow. *Quarterly Journal of the Royal Meteorological Society*, *146*(729), 1861–1879.

Santee, M., Manney, G., Livesey, N., Schwartz, M., Neu, J., & Read, W. (2017). A comprehensive overview of the climatological composition of the Asian summer monsoon anticyclone based on 10 years of Aura Microwave Limb Sounder measurements. *Journal of Geophysical Research: Atmospheres*, *122*(10), 5491–5514.

Sato, N., & Takahashi, M. (2006). Dynamical processes related to the appearance of quasi-stationary waves on the subtropical jet in the midsummer Northern Hemisphere. *Journal of Climate*, *19*(8), 1531–1544.

Siu, L. W., & Bowman, K. P. (2020). Unsteady Vortex Behavior in the Asian Monsoon Anticyclone. *Journal of the atmospheric sciences*, *77*(12), 4067–4088.

Solomon, S., Daniel, J. S., Neely, R. R., Vernier, J.-P., Dutton, E. G., & Thomason, L. W. (2011). The persistently variable "background" stratospheric aerosol layer and global climate change. *Science*, *333*(6044), 866–870.

Song, F., Zhou, T., & Wang, L. (2013). Two modes of the silk road pattern and their interannual variability simulated by lasg/iap agcm samil2. 0. *Advances in Atmospheric Sciences*, *30*(3), 908–921.

Takaya, K., & Nakamura, H. (2001). A formulation of a phase-independent wave-activity flux for stationary and migratory quasigeostrophic eddies on a zonally varying basic flow. *Journal of Atmospheric Sciences*, *58*(6), 608–627.

Tao, S. T., & Zhu, F. (1964). The 100 mb flow patterns in southern Asia in summer and its relation to the advance and retreat of the West-Pacific subtropical anticyclone over the Far East. *Acta Meteorological Sinica*, *34*(4), 385–396.

Vernier, J.-P., Fairlie, T., Natarajan, M., Wienhold, F., Bian, J., Martinsson, B., ... Bedka, K. (2015). Increase in upper tropospheric and lower stratospheric aerosol levels and its potential connection with asian pollution. *Journal of Geophysical Research: Atmospheres*, *120*(4), 1608–1619.

Vogel, B., Günther, G., Müller, R., Grooß, J., Hoor, P., Krämer, M., ... Riese, M. (2014). Fast transport from Southeast Asia boundary layer sources to northern Europe: rapid uplift in typhoons and eastward eddy shedding of the Asian monsoon anticyclone. *Atmos. Chem. Phys*, *14*(23), 12–745.

Wang, B. (1994). Climatic regimes of tropical convection and rainfall. *Journal of Climate*, 1109–1118.

Wang, B., & Fan, Z. (1999). Choice of South Asian summer monsoon indices. *Bulletin of the American Meteorological Society*, *80*(4), 629–638.

Wang, X., Wu, Y., Tung, W.-w., Richter, J. H., Glanville, A. A., Tilmes, S., ... Kinnison, D. E. (2018). The Simulation of Stratospheric Water Vapor Over the Asian Summer Monsoon in CESM1 (WACCM) Models. *Journal of Geophysical Research: Atmospheres*, *123*(20), 11–377.

Wu, L., Chou, C., Chen, C.-T., Huang, R., Knutson, T. R., Sirutis, J. J., ... Feng, Y.-C. (2014). Simulations of the present and late-twenty-first-century western North Pacific tropical cyclone activity using a regional model. *Journal of Climate*, *27*(9), 3405–3424.

Wu, Y., Orbe, C., Tilmes, S., Abalos, M., & Wang, X. (2020). Fast Transport Pathways Into the Northern Hemisphere Upper Troposphere and Lower Stratosphere During Northern Summer. *Journal of Geophysical Research: Atmospheres*, *125*(3), e2019JD031552.

Yamada, K., & Kawamura, R. (2007). Dynamical link between typhoon activity and the PJ teleconnection pattern from early summer to autumn as revealed by the JRA-25 reanalysis. *SOLA*, *3*, 65–68.

Yasui, S., & Watanabe, M. (2010). Forcing processes of the summertime circumglobal teleconnection pattern in a dry AGCM. *Journal of Climate*, *23*(8), 2093–2114.

Zhang, P., Liu, Y., & He, B. (2016). Impact of East Asian summer monsoon heating on the interannual variation of the South Asian high. *Journal of Climate*, *29*(1), 159–173.

Zhang, Q., Wu, G., & Qian, Y. (2002). The bimodality of the 100 hPa South Asia High and its relationship to the climate anomaly over East Asia in summer. *Journal of the*

Meteorological Society of Japan. Ser. II, *80*(4), 733–744.

Figure 1.

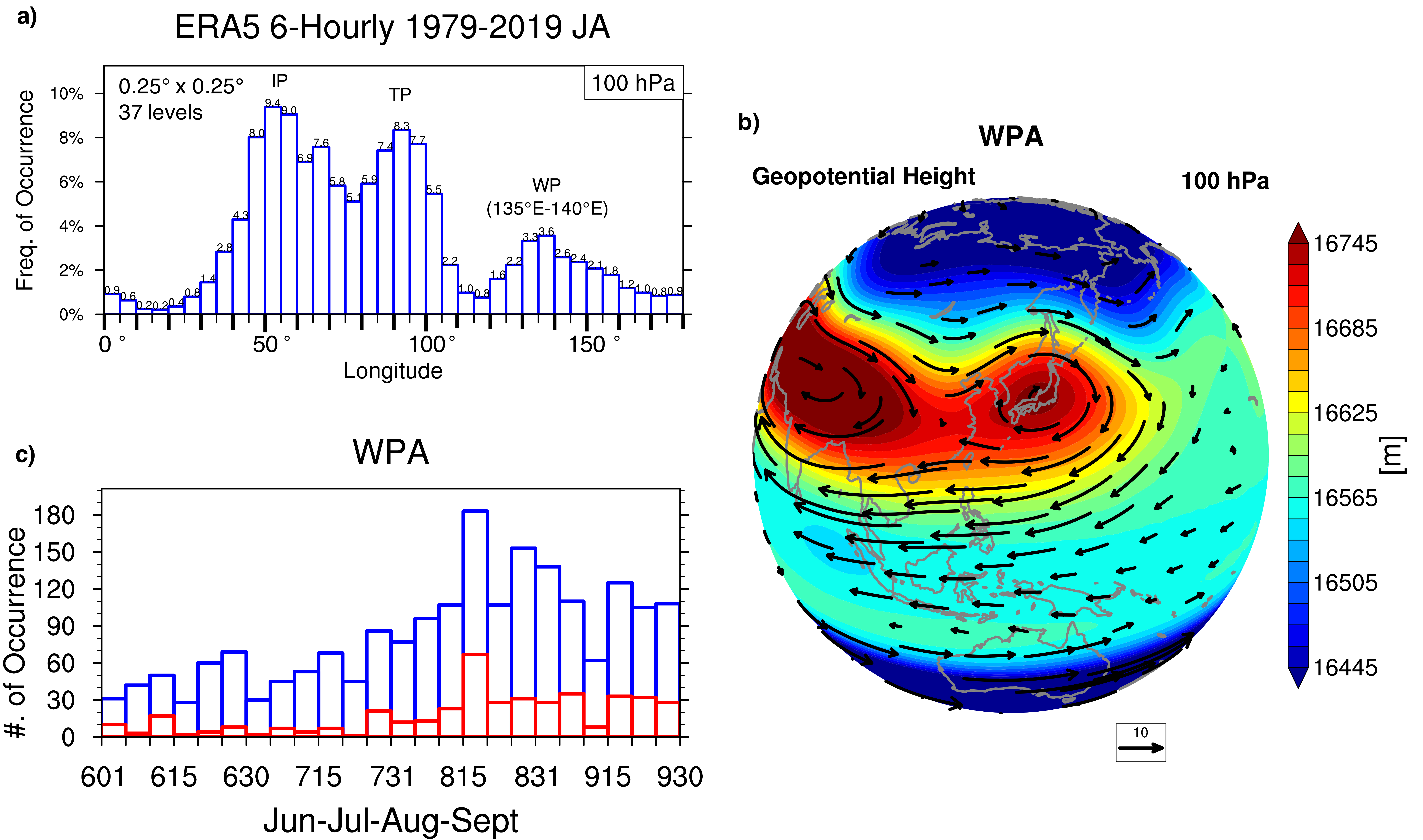
a)
ERA5 6-Hourly 1979-2019 JA
0.25° x 0.25°
37 levels
100 hPa
IP
TP
WP
(135°E-140°E)
Freq. of Occurrence
Longitude
b)
WPA
Geopotential Height
100 hPa
16745
16685
16625
16565
16505
16445
[m]
10
c)
WPA
#. of Occurrence
Jun-Jul-Aug-Sept

Figure 2.

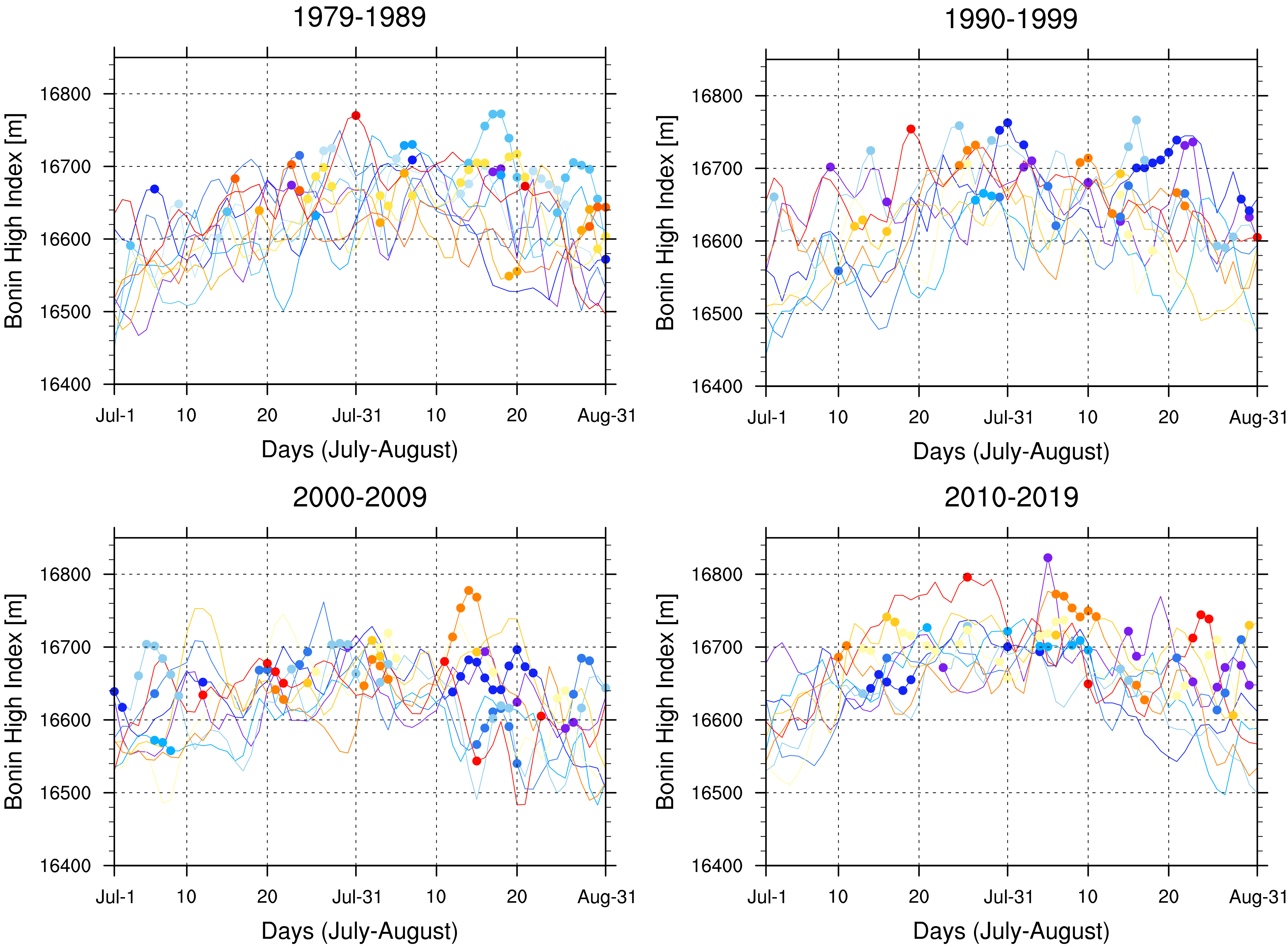

1979-1989
1990-1999
2000-2009
2010-2019
Bonin High Index [m]
16400
16500
16600
16700
16800
Jul-1
10
20
Jul-31
10
20
Aug-31
Days (July-August)

Figure 3.

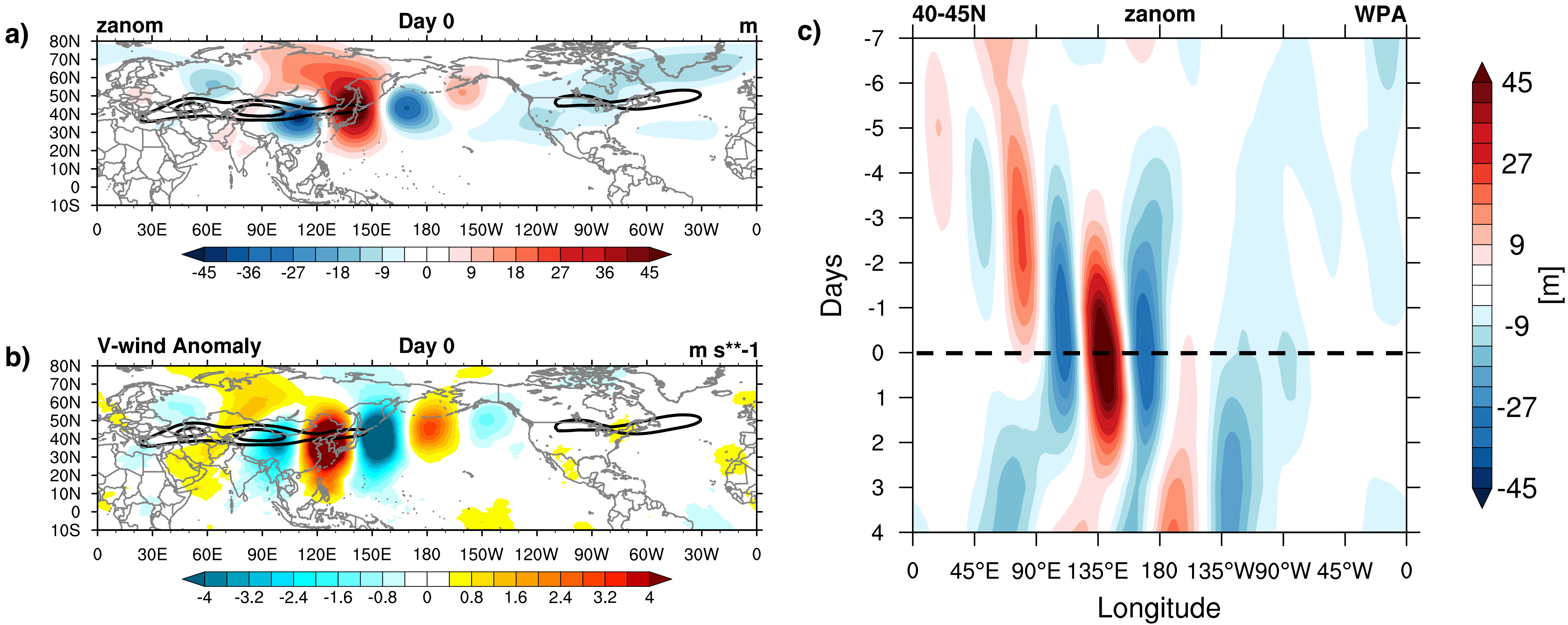

a)
zanom
Day 0
m
80N
70N
60N
50N
40N
30N
20N
10N
0
10S
0
30E
60E
90E
120E
150E
180
150W
120W
90W
60W
30W
0
-45
-36
-27
-18
-9
0
9
18
27
36
45
b)
V-wind Anomaly
Day 0
m s**-1
-4
-3.2
-2.4
-1.6
-0.8
0
0.8
1.6
2.4
3.2
4
c)
40-45N
zanom
WPA
Days
-7
-6
-5
-4
-3
-2
-1
0
1
2
3
4
0
45°E
90°E
135°E
180
135°W
90°W
45°W
0
Longitude
45
27
9
-9
-27
-45
[m]

Figure 4.

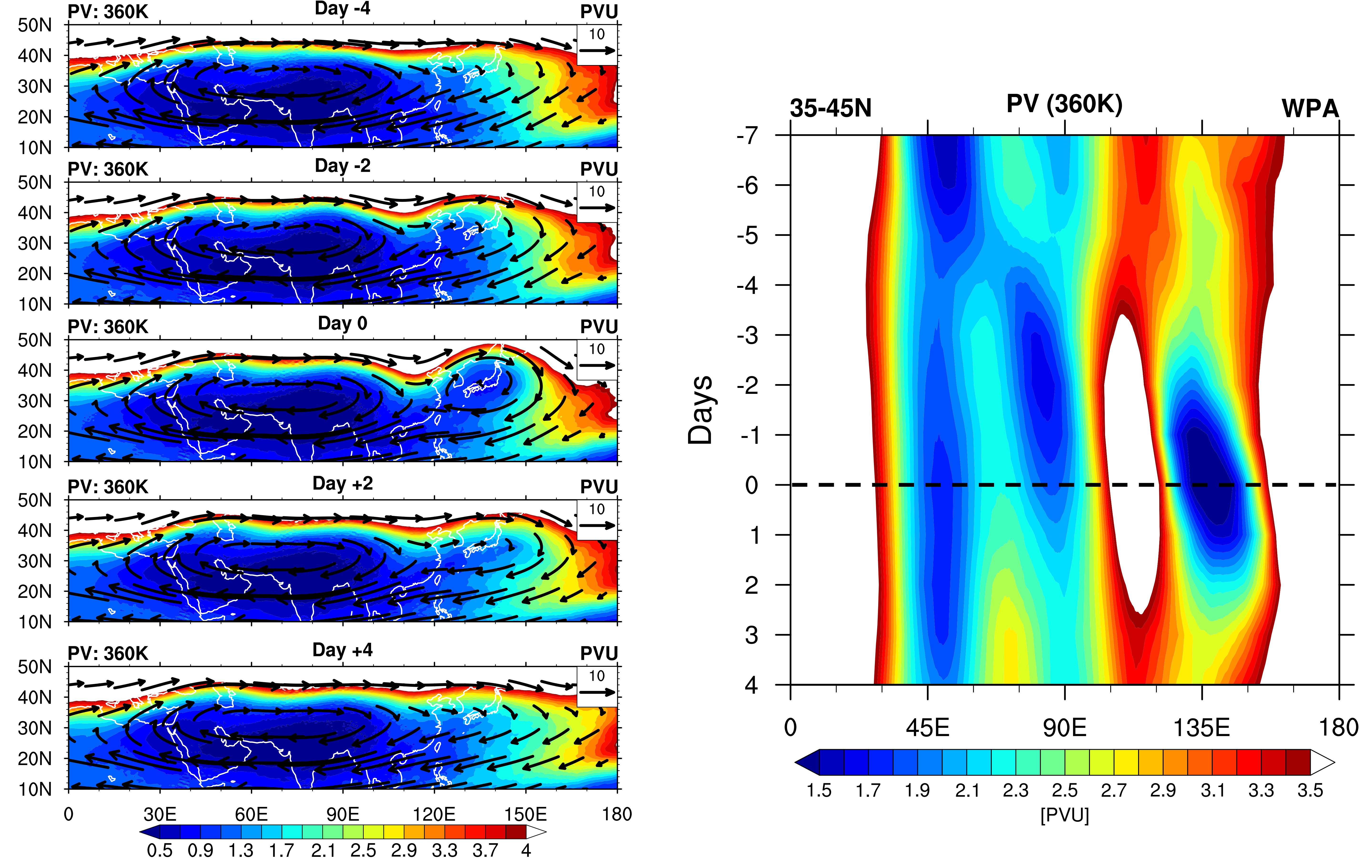

PV: 360K
Day -4
PVU
Day -2
Day 0
Day +2
Day +4
10
50N
40N
30N
20N
10N
0
30E
60E
90E
120E
150E
180
0.5
0.9
1.3
1.7
2.1
2.5
2.9
3.3
3.7
4
35-45N
PV (360K)
WPA
Days
-7
-6
-5
-4
-3
-2
-1
1
2
3
45E
135E
1.5
1.9
2.3
2.7
3.1
3.5
[PVU]

Figure 5.

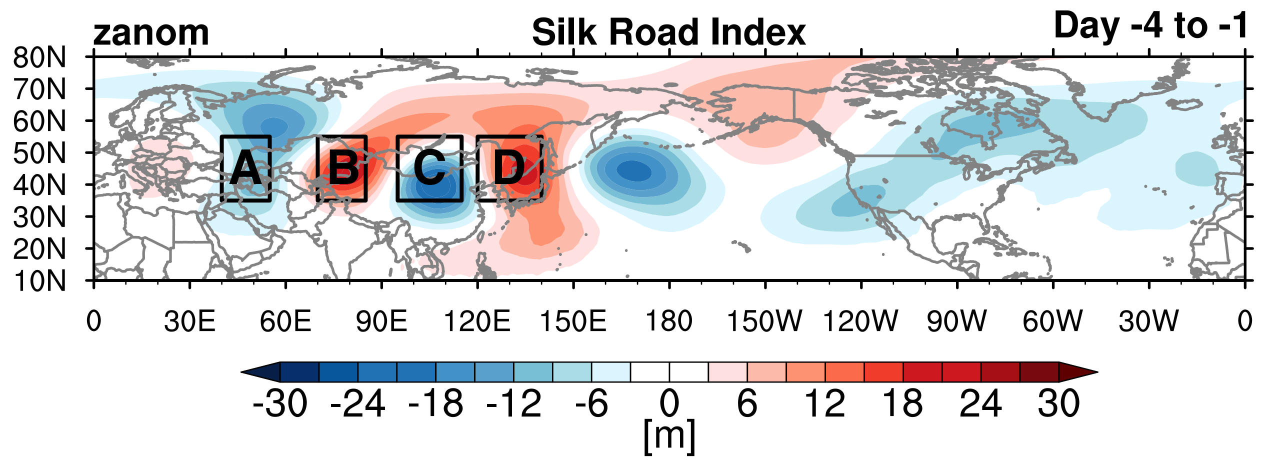
zanom
Silk Road Index
Day -4 to -1
80N
70N
60N
50N
40N
30N
20N
10N
A
B
C
D
0
30E
60E
90E
120E
150E
180
150W
120W
90W
60W
30W
0
-30
-24
-18
-12
-6
0
6
12
18
24
30
[m]

Figure 6.

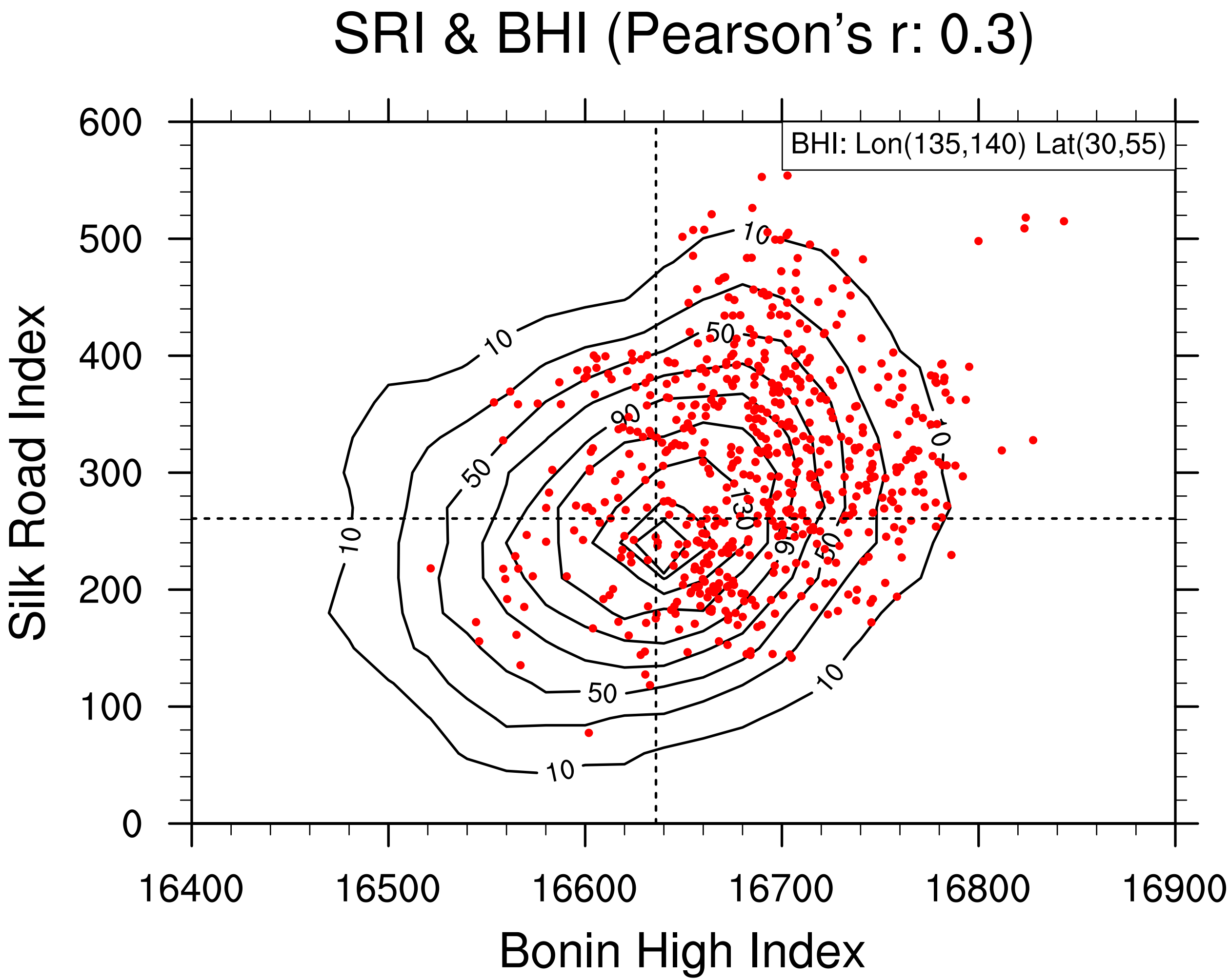
SRI & BHI (Pearson's r: 0.3)
BHI: Lon(135,140) Lat(30,55)
Silk Road Index
Bonin High Index
600
500
400
300
200
100
0
16400
16500
16600
16700
16800
16900
10
50
90
130

Figure 7.

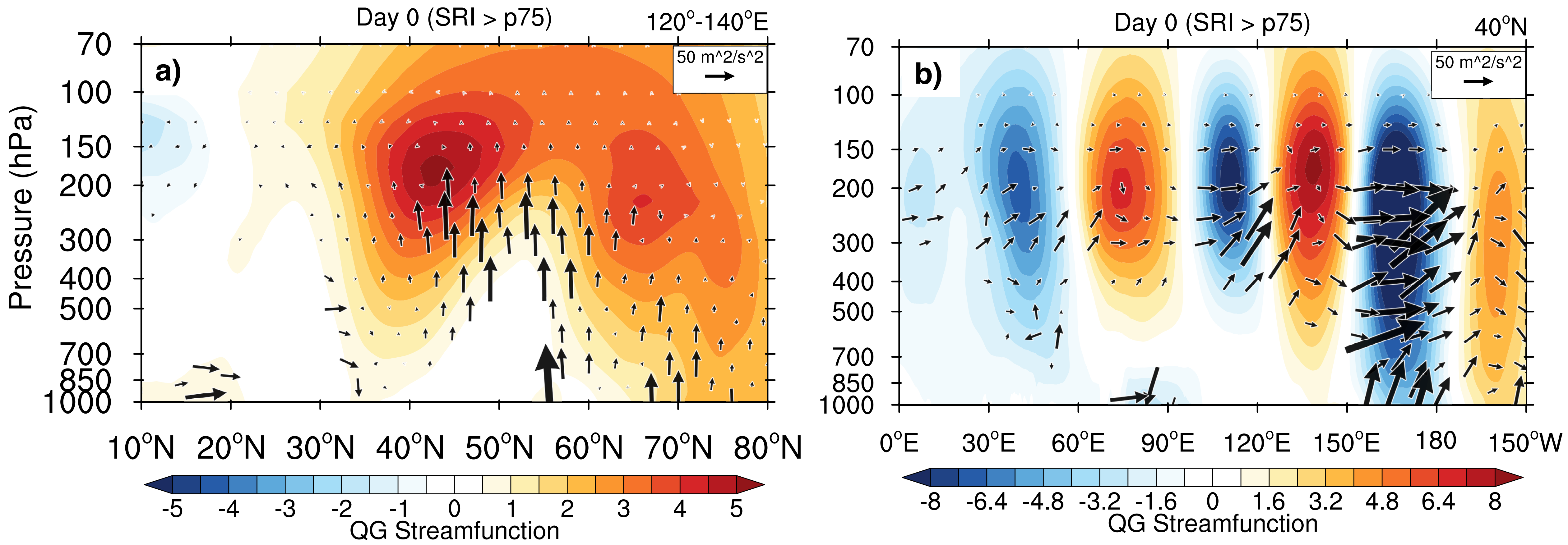

Day 0 (SRI > p75)
120°-140°E
a)
50 m^2/s^2
Pressure (hPa)
70
100
150
200
300
400
500
700
850
1000
10°N 20°N 30°N 40°N 50°N 60°N 70°N 80°N
-5 -4 -3 -2 -1 0 1 2 3 4 5
QG Streamfunction
Day 0 (SRI > p75)
40°N
b)
50 m^2/s^2
0°E 30°E 60°E 90°E 120°E 150°E 180 150°W
-8 -6.4 -4.8 -3.2 -1.6 0 1.6 3.2 4.8 6.4 8
QG Streamfunction

Figure 8.

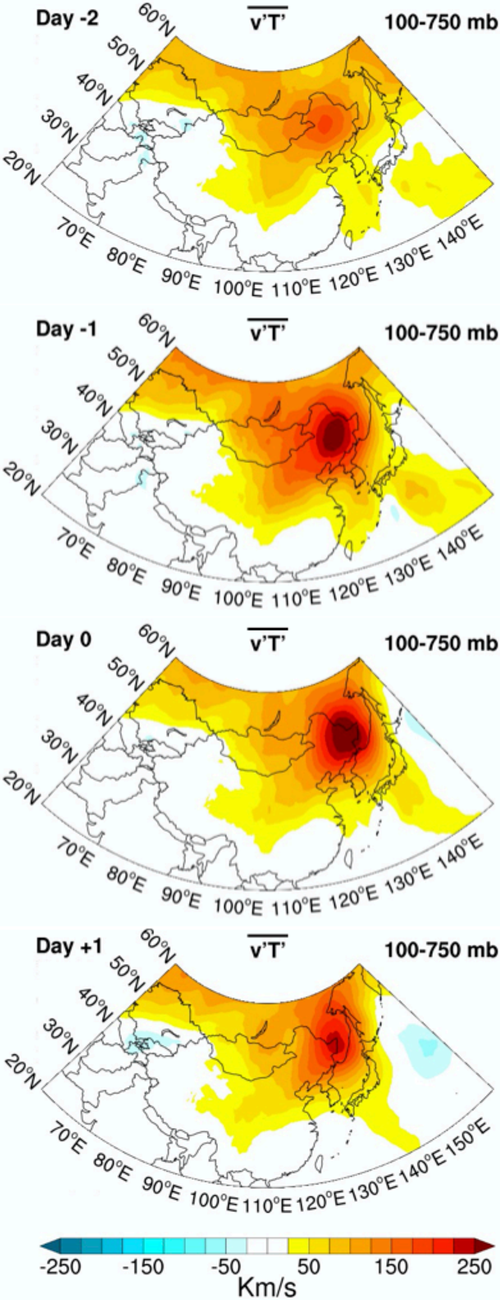
Day -2
v'T'
100-750 mb
60°N
50°N
40°N
30°N
20°N
70°E
80°E
90°E
100°E
110°E
120°E
130°E
140°E
Day -1
v'T'
100-750 mb
Day 0
v'T'
100-750 mb
Day +1
v'T'
100-750 mb
150°E
-250
-150
-50
50
150
250
Km/s

Figure 9.

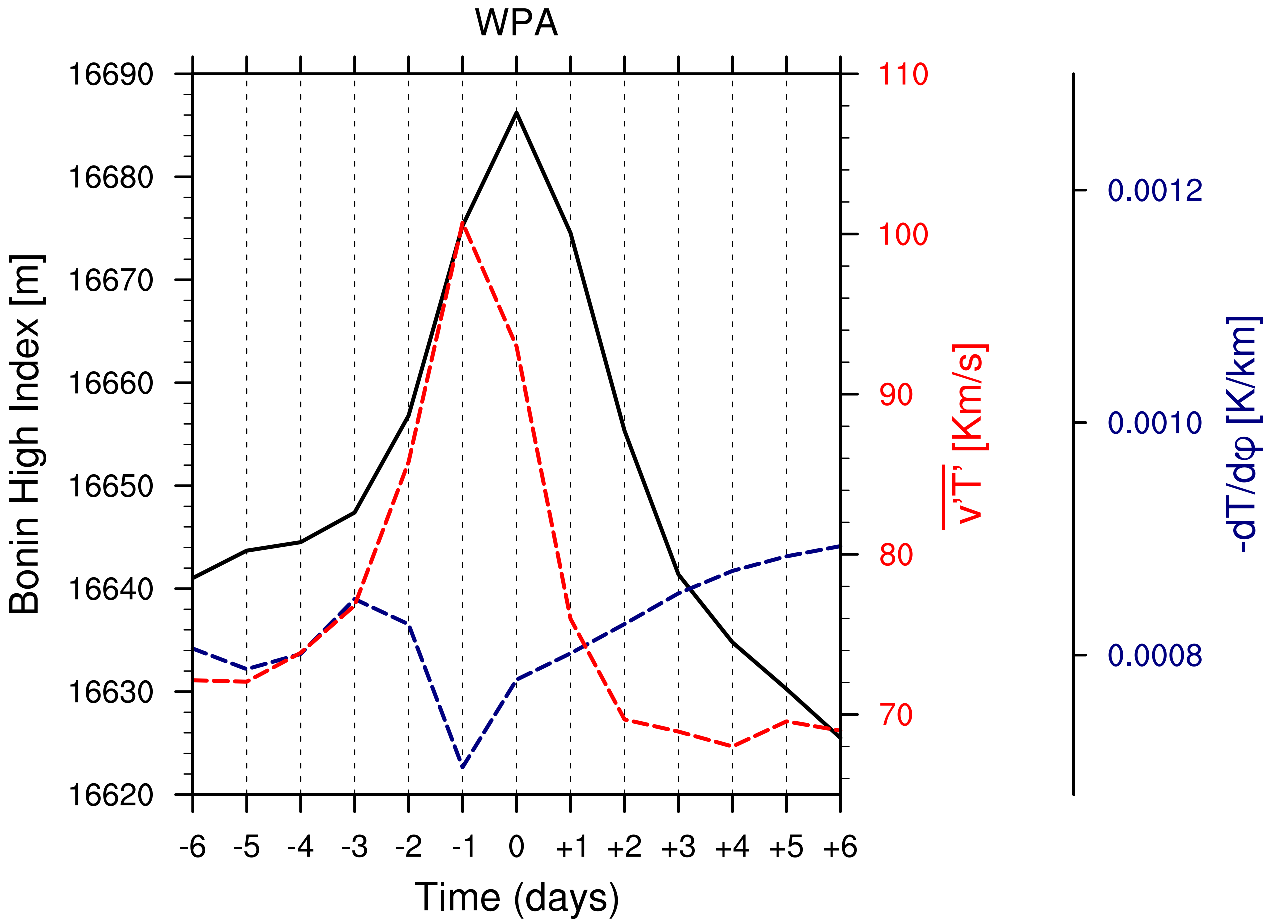

WPA
Bonin High Index [m]
16690
16680
16670
16660
16650
16640
16630
16620
110
100
90
80
70
$\overline{v'T'}$ [Km/s]
0.0012
0.0010
0.0008
-dT/dφ [K/km]
-6
-5
-4
-3
-2
-1
0
+1
+2
+3
+4
+5
+6
Time (days)

Figure 10.

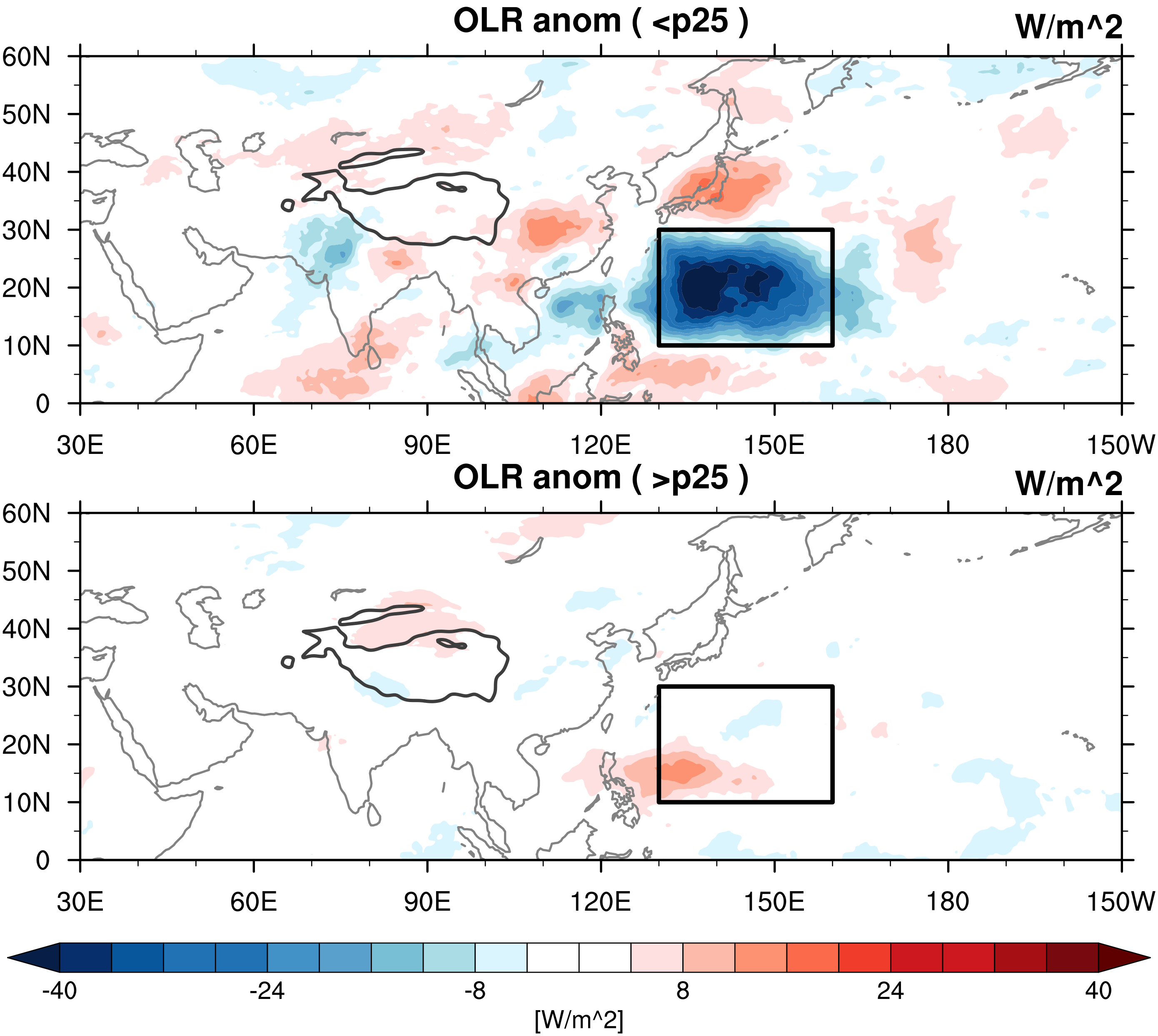

OLR anom (<p25)
W/m^2
60N
50N
40N
30N
20N
10N
0
30E
60E
90E
120E
150E
180
150W
OLR anom (>p25)
W/m^2
60N
50N
40N
30N
20N
10N
0
30E
60E
90E
120E
150E
180
150W
-40
-24
-8
8
24
40
[W/m^2]

Figure 11.

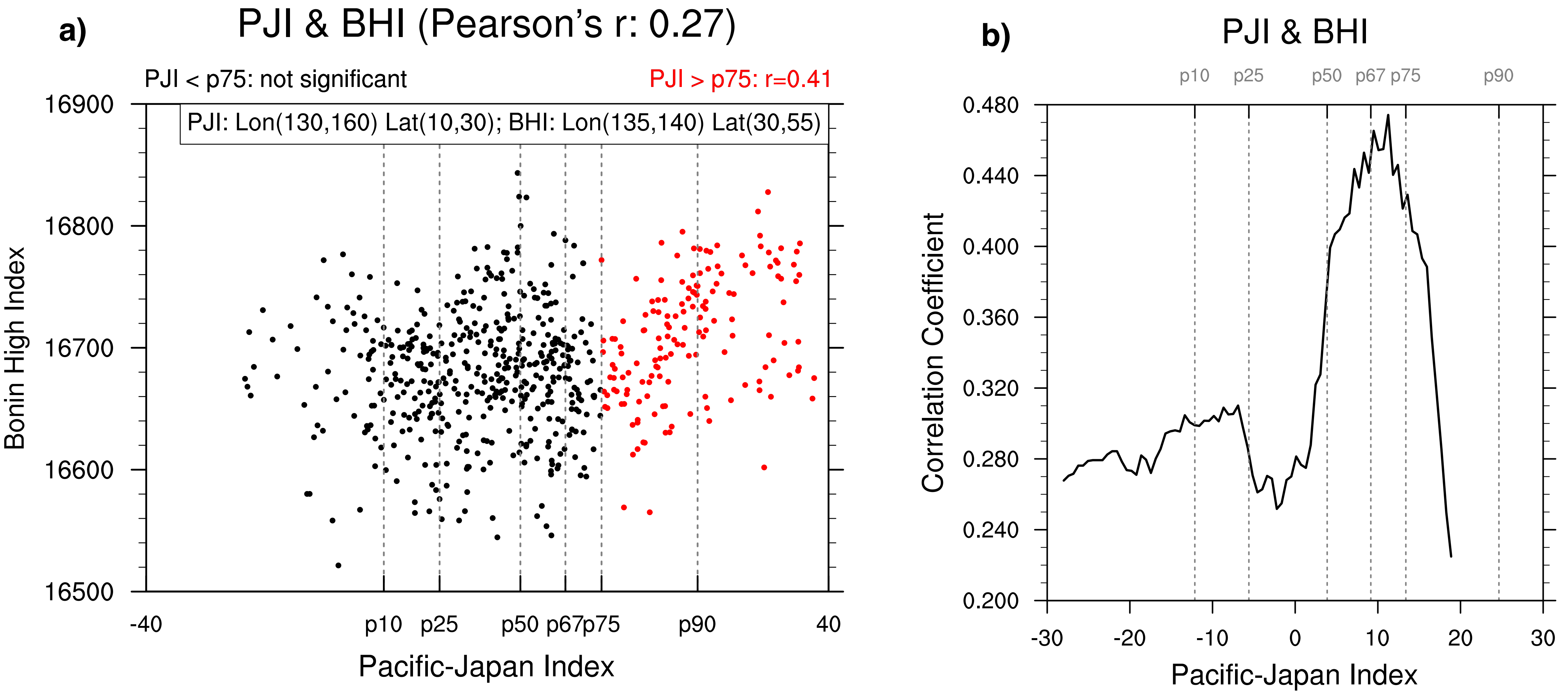
a)
PJI & BHI (Pearson's r: 0.27)
PJI < p75: not significant
PJI > p75: r=0.41
PJI: Lon(130,160) Lat(10,30); BHI: Lon(135,140) Lat(30,55)
Bonin High Index
16900
16800
16700
16600
16500
-40
p10
p25
p50
p67
p75
p90
40
Pacific-Japan Index
b)
PJI & BHI
p10
p25
p50
p67
p75
p90
Correlation Coefficient
0.480
0.440
0.400
0.360
0.320
0.280
0.240
0.200
-30
-20
-10
0
10
20
30
Pacific-Japan Index

Figure 12.

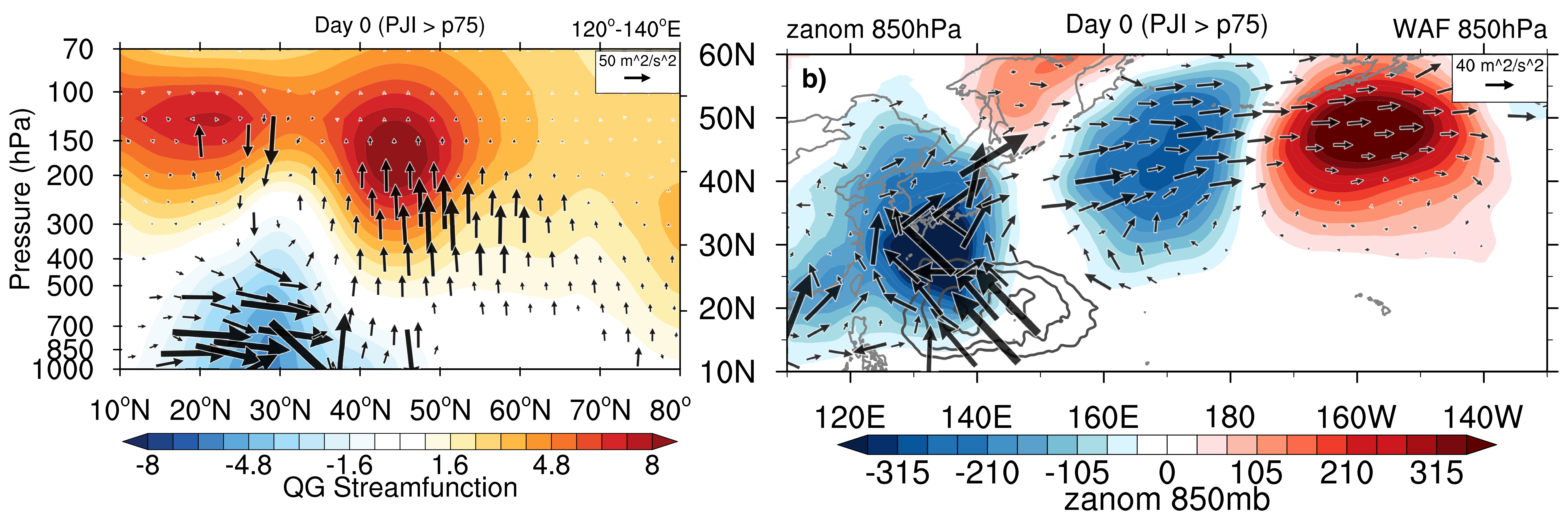

Day 0 (PJI > p75)
120°-140°E
50 m^2/s^2
Pressure (hPa)
70
100
150
200
300
400
500
700
850
1000
10°N
20°N
30°N
40°N
50°N
60°N
70°N
80°
-8
-4.8
-1.6
1.6
4.8
8
QG Streamfunction
zanom 850hPa
Day 0 (PJI > p75)
WAF 850hPa
b)
40 m^2/s^2
60N
50N
40N
30N
20N
10N
120E
140E
160E
180
160W
140W
-315
-210
-105
0
105
210
315
zanom 850mb